Solar Phys (2020) 295:55
https://doi.org/10.1007/s11207-020-01619-x

A Geoeffective CME Caused by the Eruption of a Quiescent Prominence on 29 September 2013

V.V. Grechnev[1] · **I.V. Kuzmenko**[2]

Received: 11 December 2019 / Accepted: 28 March 2020

Abstract The eruption of a large prominence that occurred away of active regions in the SOL2013-09-29 event produced a fast coronal mass ejection (CME) and a shock wave. The event caused considerable geospace disturbances, including a proton enhancement that have been addressed in previous studies. Continuing with the analysis of this event, we focus on the development of the CME and shock wave, assess an expected geospace impact using simplest considerations, and compare the expectations with in situ measurements near Earth. The high CME speed in this non-flare-associated event was determined by a considerable reconnected flux that corresponds to a pattern established by different authors. Estimations based on a few approaches showed the reconnection flux in this event to be comparable with a typical value in flare-associated eruptions. The shock wave was most likely impulsively excited by the erupting prominence in the same way as in flare-associated events and changed to the bow-shock regime later. The trajectory calculated for this scenario reproduces the Type II emission observed from 30 MHz to 70 kHz; its interruptions were probably caused by propagation effects. Properties of the near-Earth proton enhancement are discussed considering the results of recent studies.

Keywords Coronal mass ejections · Energetic particles · Magnetic fields · Prominences, active · Radio bursts, Type II · Solar wind, disturbances · Waves, shock

Electronic supplementary material The online version of this article (https://doi.org/10.1007/s11207-020-01619-x) contains supplementary material, which is available to authorized users.

✉ V.V. Grechnev
grechnev@iszf.irk.ru

I.V. Kuzmenko
kuzmenko_irina@mail.ru

[1] Institute of Solar-Terrestrial Physics SB RAS, Lermontov St. 126A, Irkutsk 664033, Russia

[2] Institute of Applied Astronomy RAS, Kutuzov Emb. 10, St. Petersburg 191187, Russia

Published online: 17 April 2020

1. Introduction

Coronal mass ejections (CMEs) and associated processes are the main sources of space-weather disturbances such as solar energetic particles (SEPs), geomagnetic disturbances, Forbush decreases of the cosmic-ray intensity, and others. When an interplanetary CME (ICME: e.g. Richardson and Cane, 2010; Manchester *et al.*, 2017) approaches Earth, a geomagnetic disturbance and/or a Forbush decrease can occur. The geomagnetic disturbance is considerably stronger, if the ICME is fast and carries a southward (negative) magnetic B_z component. The depth of a Forbush decrease does not depend on the magnetic-field direction.

Traditionally, two categories of flare-associated and non-flare-associated CMEs have been identified, depending on the presence or absence of conspicuous chromospheric flare emissions (e.g. in the Hα line or in the 1600 Å ultraviolet channel) that accompanies the CME development (e.g. MacQueen and Fisher, 1983; Švestka, 2001). Flare-associated CMEs develop in eruptions from active regions, undergo rapid, strong acceleration, and have nearly constant speeds in the fields of view of coronagraphs. Non-flare-associated CMEs typically develop after eruptions of large "quiescent" filaments (prominences) away from active regions; their acceleration stage lasts much longer, being usually observed by coronagraphs.

Flare-associated CMEs usually can reach considerably higher speeds than non-flare-associated CMEs. Shock waves expand ahead of fast CMEs. Shock waves and flares have been considered as the probable sources of SEPs that can be accelerated to high energies, being dangerous for equipment and astronauts onboard spacecraft. SEPs mostly appear in association with flares and fast CMEs that makes difficult to determine the role of each possible particle accelerator. Consensus has not been reached about their contributions to the SEP production (e.g. Klein and Trottet, 2001; Kallenrode, 2003; Reames, 2013; Grechnev *et al.*, 2015a, 2017; Kahler *et al.*, 2017; Cliver *et al.*, 2019).

Having been born in active regions, where magnetic fields are strong, flare-associated CMEs are heavily magnetized and, being mostly faster, can potentially cause stronger space-weather disturbances. Indeed, the sources for the majority of intense geomagnetic storms with Dst < -100 nT that occurred during Solar Cycle 23 were CMEs originating in active-region eruptions associated with flares. Nevertheless, the primary sources for a few intense geomagnetic storms observed during this period were prominence eruptions away from active regions (see, e.g., Chertok *et al.*, 2013). Moreover, non-active-region eruptions occasionally produce considerable SEP events (e.g. Chertok, Grechnev, and Meshalkina, 2009; Gopalswamy *et al.*, 2015; Cliver *et al.*, 2019).

Analyzing intense geomagnetic storms of Solar Cycle 23, Chertok *et al.* (2013, 2015) found statistical relations between the total magnetic flux involved in an active-region eruption and such parameters of the associated geospace disturbance as the Sun–Earth transit time, the depth of the Forbush decrease, and the strength of the geomagnetic disturbance in terms of the Dst and ap indices. In particular, an inverse dependence on the erupted magnetic flux was found for the Sun–Earth transit time, consistent with a direct relation between the magnetic flux and CME speed (Qiu and Yurchyshyn, 2005; Pal *et al.*, 2018). Non-active-region eruptions mostly followed these patterns, although their magnetic fluxes seem to have been underestimated by Chertok *et al.* (2013) by a factor of 1.2 – 2.0 that we found, considering the transit time and Forbush decrease. It is difficult to state the underestimation with confidence, because the number of non-active-region eruptions analyzed in this study was as small as seven events. Nevertheless, the magnetic-flux underestimation is probable for such eruptions, because the algorithms and quantitative criteria that are used to detect surface

activity in flare-associated events may not be optimal for non-flare-associated eruptions that develop longer, involve weaker magnetic fields distributed over larger areas, and produce much weaker emissions.

We address a geoeffective event, whose solar source was associated with a non-active-region eruption of a large filament on 29 September 2013 (hereafter Sep29 event). The eruption gave rise to a fast CME with an average speed of 1180 $\mathrm{km\,s^{-1}}$. Several aspects of this event and its space-weather impact have been extensively studied, mostly along with different events. Holman and Foord (2015) addressed a unique case of an X-ray flare associated with a quiescent-filament eruption and discussed its possible triggering by the magnetic-flux emergence. Li, Zhang, and Ji (2015) and Palacios *et al.* (2015) analyzed the flux emergence and activation of the filament. The CME orientation and configuration were determined by Wood *et al.* (2016) and Bothmer and Mrotzek (2017) based on three-dimensional (3D) model reconstructions from the CME images obtained at three vantage points of the Solar and Heliospheric Observatory (SOHO: Domingo, Fleck, and Poland, 1995) and the twin-spacecraft Solar-Terrestrial Relations Observatory (STEREO: Kaiser *et al.*, 2008). These studies also addressed the corresponding ICME and its ionospheric and magnetospheric impact. Gopalswamy *et al.* (2015) and Cliver *et al.* (2019) considered the proton enhancements produced by this event and a few other non-flare-associated events. Al-Hamadani, Pohjolainen, and Valtonen (2017) analyzed long-wave Type II emissions produced by shock waves associated with this CME and several others.

Nevertheless, some aspects of the Sep29 event remain unclear. These are, for example, the CME development and the overall history of the associated shock wave, which was presumed in previous studies to be excited by the super-Alfvénic CME (e.g. Gopalswamy *et al.*, 2015). The most challenging question is why this non-flare-associated CME was so fast. We also compare some parameters of space-weather disturbances caused by this event with expectations from the statistical patterns found by Chertok *et al.* (2013, 2015) for the events of Solar Cycle 23 that were elaborated by Chertok, Grechnev, and Abunin (2017) for the usage of data from the Solar Dynamics Observatory (SDO) in Solar Cycle 24.

Analyzing this particular event, we hope to shed additional light on non-active-region eruptions. As mentioned, there are indications of a possible underestimation of the erupted magnetic flux in such events. Conversely, Cliver *et al.* (2019) argued that the magnetic flux involved in the Sep29 eruption and in other non-flare-associated SEP-productive events was low. To find which of these contradicting indications is more realistic, we pay special attention to the erupted magnetic flux. We also endeavor to estimate parameters of the CME and its expected geoeffective impact from simple considerations without 3D model reconstructions to extend the opportunities of space-weather prediction.

Section 2 overviews the solar eruptive event and its space-weather consequences. Section 3 addresses the filament eruption and CME development, particularly their kinematics. Section 4 considers manifestations of the shock wave in dynamic radio spectra and solar images and reveals its overall history. Section 5 addresses the magnetic flux involved in the eruption. Section 6 considers the ICME, the geospace disturbances that it produced, and the near-Earth proton enhancement. Section 7 summarizes the conclusions. The movies in the Electronic Supplementary Material illustrate the observations and measurements.

2. Overview of the Solar Event and Its Space-Weather Impact

A long inverse-S-shaped filament was observed in the northern solar hemisphere in 304 Å images produced by the Atmospheric Imaging Assembly (AIA: Lemen *et al.*, 2012) on board

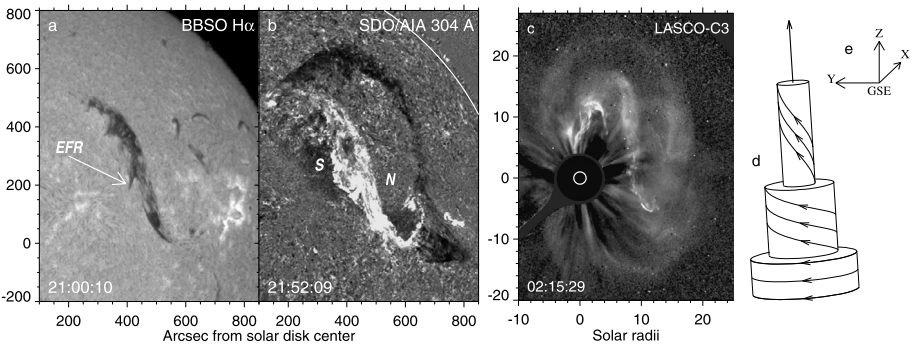

Figure 1 (**a**) The filament in the activated state as observed in the Hα line shortly before the eruption. The arrow labeled EFR points at the emerging-flux region. (**b**) Filament eruption and ribbons observed by SDO/AIA in 304 Å. Labels S and N indicate magnetic polarities. (**c**) CME observed by SOHO/LASCO-C3. The small circle denotes solar limb. (**d**) Expected orientation and magnetic structure of the erupted flux rope. (**e**) The axes in the GSE system.

SDO starting from its rotation onto the Earth-facing solar surface on 21 September 2013. The filament observed in the Big Bear Solar Observatory (BBSO) in the Hα line seems to comprise three segments (Figure 1a). One segment spanned from the southern filament's end to a long barb pointed by the arrow. Another segment connected this barb with the thickest northerly barb. The third segment extended farther northeast. Holman and Foord (2015), Li, Zhang, and Ji (2015), and Palacios *et al.* (2015) established that the filament was activated on 29 September by the magnetic-flux emergence beneath the long barb that lasted several hours. Reconnection between the emerging dipole and magnetic fields of the filament caused a C1.2 soft X-ray (SXR) flare and triggered reconnection along the filament. We note that Hα images and a movie available at the BBSO Web site (www.bbso.njit.edu) show the development of a helical structure in the activating filament (see the northern part of the middle segment in Figure 1a) that indicates progressive transformation by reconnection of its sheared magnetic structure into a flux-rope progenitor.

After 21:00 (*all times hereafter refer to UTC*), the filament eruption started. Figure 1b shows a dark erupting filament and its bright post-eruption footprint (ribbons) below, whose shape is inverse-S-like, indicating the left handedness of the filament (for different ways to find the handedness see, e.g., Grechnev *et al.*, 2019). The line-of-sight magnetograms produced by the Helioseismic and Magnetic Imager (HMI: Scherrer *et al.*, 2012) on board SDO reveal the magnetic polarities of the adjacent regions that are indicated in Figure 1b. The filament accelerated relatively gradually, remaining in the AIA field of view until 22:10.

The eruption led to a fast CME with a nearly constant speed of 1180 km s^{-1} and weak deceleration of -5.3 m s^{-2} according to the online CME catalog (cdaw.gsfc.nasa.gov/CME_list/: Yashiro *et al.*, 2004). The kinematics is typical of flare-associated CMEs. Figure 1c shows the CME five hours after the eruption onset. The CME had a complex structure with a segmented core that developed from the eruptive filament. The tilt of the longest core segment to the solar axis decreased relative to the initial orientation of the filament. The segments and their shell (the frontal structure) were displaced westward from the solar disk. From the CME orientation one might expect for the corresponding ICME either to miss Earth, as Wood *et al.* (2016) found to be probable, or to hit Earth by its eastern edge, as Bothmer and Mrotzek (2017) concluded.

Figures 1b and 1c imply the magnetic structure and orientation of the flux rope and tentative expectations for the variations of magnetic components in the Earth orbit that are often

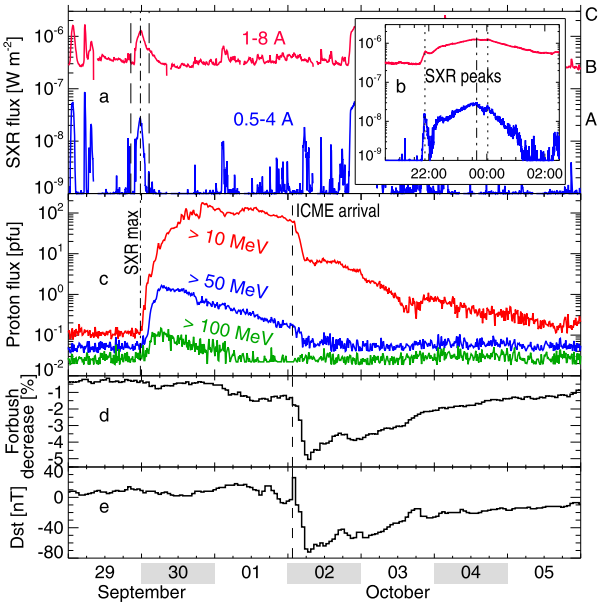

Figure 2 Temporal profiles of the solar event and space-weather disturbances that it caused. (**a**) SXR flux measured by GOES (five-minute average). The vertical dash-dotted lines in panels **a** – **c** mark the main SXR peak. The vertical dashed lines denote the interval shown in the inset. (**b**) Expanded GOES light curves (ten-second average). The vertical dash-dotted and dotted lines mark three SXR peaks. (**c**) Proton flux in three standard integral proton channels (15-minute average). The vertical dashed line in panels **c** – **e** marks the onset of the disturbance on 2 October at 01:30. (**d**) Forbush decrease at 10 GV rigidity (Courtesy A.V. Belov). (**e**) Variations of the hourly geomagnetic Dst index.

measured in the GSE system (Figure 1e). Figure 1d shows the scheme of a left-handed force-free cylindrical flux rope, whose orientation is determined by the magnetic-field direction by sides of the eruption region and the tilt of the CME core. As mentioned, if the corresponding magnetic cloud (MC) hits Earth, then it does by its eastern edge. In this situation, the B_z component is expected to be initially insignificant and become positive inside the MC. B_y is expected to be small, being positive in the MC leading half and negative in its trailing half. B_x is expected to be the largest and always positive. The geomagnetic storm that this MC may cause is not expected to be severe.

The light curves of a long-duration C1.2 SXR flare associated with the eruption are shown in Figure 2a and, in more detail, in the inset (Figure 2b). The broken lines denote three peaks that are discernible in the 0.5 – 4 Å GOES channel at 21:52, at 23:40 (reported peak), and a minor peak at 00:00 on 30 September. Soft X-rays were emitted by a large post-eruption arcade that is detectable until at least 06:30 on 30 September in the 193 Å and 211 Å AIA channels. The ribbons at the base of the arcade are also visible in 304 Å, while their faint parts only are barely detectable in 1600 Å by 23:00 on 29 September.

Figures 2c – 2e present space-weather disturbances caused by the solar event: a near-Earth proton enhancement up to 180 pfu (1 pfu = 1 particle cm^{-2} s^{-1} ster^{-1}) in the $>$ 10 MeV integral proton channel and up to 0.14 pfu in the $>$ 100 MeV channel (Figure 2c), a Forbush decrease down to 4.6% (Figure 2d), and a moderate geomagnetic storm with a minimum Dst = −72 nT (Figure 2e). The values of the Forbush decrease at 10 GV rigidity were calculated by A.V. Belov with colleagues in IZMIRAN from the data provided by the worldwide neutron-monitor network. The final hourly Dst index is provided by the World Data Center for Geomagnetism, Kyoto at wdc.kugi.kyoto-u.ac.jp/dstdir/index.html.

The geomagnetic disturbance and Forbush decrease associated with the arrival of the ICME launched on 29 September started on 2 October around 01:30. The Dst index rapidly reached a minimum on 2 October at 08:00. The ICME arrival is also marked by a decrease in the proton flux in Figure 2c that appears as a low-energy analog of the Forbush decrease.

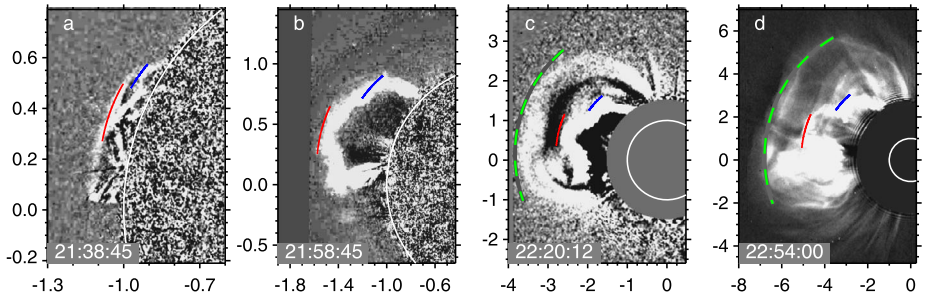

Figure 3 Prominence eruption and CME development in the STEREO-A images: **a**, **b**) EUVI 304 Å, **c**) COR1, **d**) COR2. The blue arc outlines the northern segment. The red arc outlines the middle segment. The dashed-green arc outlines the frontal structure. The white circle represents solar limb. The axes show solar radii from solar-disk center.

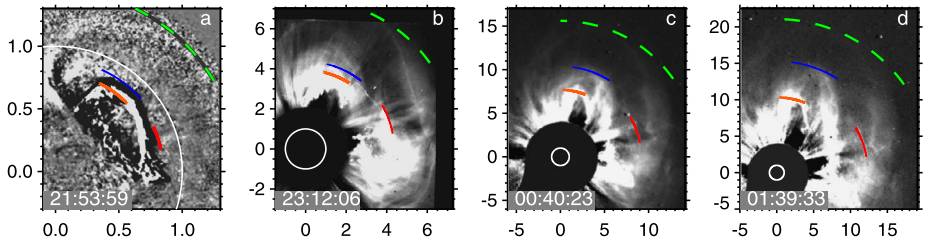

Figure 4 Prominence eruption and CME development observed from the Earth's direction: **a**) SDO/AIA 211 Å; **b**) SOHO/LASCO-C2; **c**, **d**) SOHO/LASCO-C3. The notations are the same as in Figure 3. The orange arc (northward from the red arc) represents the measurements by Gopalswamy *et al.* (2015).

Note that a shallow Forbush decrease started at least two days earlier that suggests the passage of a preceding slow ICME, whose source is not known. A possible additional milestone of the disturbance is indicated by the changes in the > 10 MeV proton flux, cosmic-ray level, and the Dst index on 3 October around 19:00.

3. Solar Eruption and CME

3.1. Eruptive Filament and CME Development

The prominence eruption and CME development were observed in various spectral ranges from different directions by SDO and SOHO; by STEREO-A located 147° westward from the Sun–Earth line; and by STEREO-B located 139.5° eastward from it. The erupting prominence and CME observed from STEREO-A are shown in Figure 3. SDO/AIA and SOHO/LASCO images are shown in Figure 4. The movies in the Electronic Supplementary Material, STEREO-A_fs.mpg, AIA_LASCO_fs.mpg, and AIA_LASCO_core.mpg present the event in detail.

A slow rise of the prominence (filament) started around 21:12, and then its liftoff accelerated. The prominence expansion was not uniform; its southernmost part in Figures 1b and 3b and the movies was most active. SDO/AIA 304 Å images (e.g. Figure 1b) reveal long flare-like ribbons that developed during the prominence eruption. The AIA channels that are

dominated by iron emission lines show the development of a long-lived arcade. A minor activity episode around 23:46 is indicated by motions of brightened loops around [500″, 100″], southerly from the X-ray source addressed by Holman and Foord (2015).

A STEREO-A/EUVI 304 Å difference image in Figure 3a reveals in the structure of the erupting prominence three segments, whose ends are rooted to the solar surface. The main bodies of the segments get combined into a joint structure in Figure 3b. This transformation is reminiscent of the dual-filament CME initiation model (Uralov *et al.*, 2002; Grechnev *et al.*, 2006), where this occurs due to reconnection between the segments and between the filament threads, detaching them from their bases. The observations in the Hα line mentioned in the preceding section and Holman and Foord's (2015) conclusions about reconnection support this scenario. Some connections of each segment to the solar surface survived that is indicated by a segmented structure of the CME core in Figures 3c, 3d and 4c, 4d, where the blue arc outlines the northern segment and the red arc outlines the middle segment. This outcome indicates partial reconnection that is expected in a real situation, where magnetic fields are complex and tangled. The fast southern part of the core and faint loops ahead of its northern segment filled the cavity during 22:15 – 22:40 in Figures 3c, 3d, and 4b. The nonuniform expansion of different parts of the core caused the change in the shape of the frontal structure (FS) from nearly circular in Figure 3c to a dipped in Figure 3d.

The SDO/AIA 211 Å image in Figure 4a reveals a faint shell (outlined with the dashed-green arc) that enveloped the erupting prominence and later became the FS that is faintly visible in Figures 4b – 4d. The figures and Electronic Supplementary Material show that the changes in the CME continued. After 23:30, the northern segment of the core divided, the outer part stretched and expanded faster than the inner part. The core took an inverse-S-like shape, and its middle part became nearly parallel to the solar rotation axis (cf. Figure 1c). As the observations indicate, the initial structural features of the eruptive prominence determined the behavior of the core, whose outward pressure affected the FS.

3.2. Plane-of-the-Sky Kinematics of the Prominence and CME

Gopalswamy *et al.* (2015) measured distance–time plots for the erupting prominence and the CME leading edge and core. Using the polynomial fit of the first and second order to the measured points, the authors estimated the average velocities and accelerations for the erupting prominence, the fastest detectable feature at the CME leading edge, and for the slower northern segment of the core that was apparently associated with the erupting prominence, as the measurements confirmed. The CME leading edge had an average velocity of 1180 km s^{-1} and an average deceleration of -5.4 m s^{-2}. These measurements are probably related to a wave trace ahead of the CME body to be discussed in Section 4.3. The core had an average velocity of 505 km s^{-1} and an average acceleration of $+5.4$ m s^{-2}. On the other hand, the method used by the authors does not reveal the temporal profile of the acceleration that is important to analyze the development of the eruption and CME. This is a subject of our measurements.

We measured the kinematics for different parts of the erupting prominence and CME from STEREO-A images, because the overlap between the EUVI and COR1 observations facilitates identifying the structures visible in the extreme ultraviolet (EUV) and white light. STEREO-B images only show the FS and northern part of the core. The higher-resolution SDO/AIA images allowed us to measure the erupting prominence until about 22:15, when it left the AIA field of view. The measurements from SDO/AIA and SOHO/LASCO images that present observations from the Earth's direction were linearly transformed to match the measurements from the STEREO-A vantage point. The measurements from STEREO-B images were handled in a similar way.

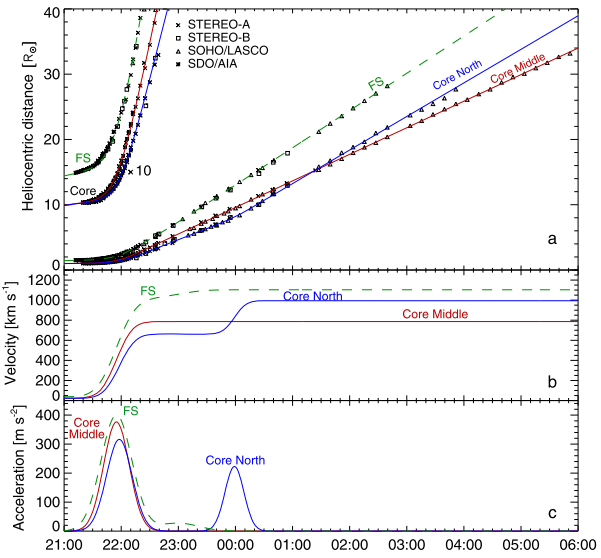

Figure 5 Kinematics measured for the northern and middle segments of the prominence and CME core and for the FS in the plane of the sky as viewed from STEREO-A. **a**) Distance–time plot. The symbols represent the initial manual measurements. The curves represent the analytic fit of the measured points. The upper-left region shows the initial portions of the plots magnified by a factor of ten. **b**) Velocity–time plots. **c**) Acceleration–time plots.

The symbols in Figure 5a present the initial manual measurements. The errors estimated subjectively are 5 – 10 Mm for the erupting prominence and 20 Mm for the shell measured in EUV images, 50 Mm for the CME components measured in STEREO/COR1 and LASCO-C2 images, and 150 – 200 Mm for the core and 200 – 300 Mm for the FS measured in STEREO/COR2 and LASCO-C3 images.

To evaluate the velocities before an acceleration episode and after it, we use a linear fit of the initial distance–time measurements within the constant-velocity intervals. The scatter in the distance–time points determines the accuracy of the velocity estimates that is within 2.5% (1σ level) for the Sep29 CME components and does not affect the velocity temporal profile.

The area of an acceleration pulse is determined by the velocities, while its real shape is difficult to reveal from observations. Its fine structure is not expected because of a huge size of the prominence and limited propagation speed of a magnetohydrodynamic (MHD) disturbance that is responsible for the eruption process. To find the acceleration, we assign it a Gaussian shape and adjust its parameters to approach the best fit of the double-integrated acceleration temporal profile to the distance–time points measured. If two or more acceleration episodes are present, then a combination of Gaussian acceleration pulses is used.

Then we produce a set of resized images, whose field of view changes according to the analytic distance–time fit. When viewing the set of resized images as a movie, the structure of interest should remain static. If this is not the case, the parameters of the fit are refined. This approach was used in several previous studies (e.g. Grechnev *et al.*, 2014, 2015b, 2016; Kuzmenko and Grechnev, 2017).

The kinematical curves fitted analytically for different parts of the erupting prominence and CME are shown in Figure 5 by the curves, whose colors and line styles correspond to Figures 3 and 4. The middle part of the core and the FS underwent the main acceleration nearly simultaneously at heliocentric distances of about 1.5 $R_\odot$ and 2.3 $R_\odot$, respectively. The heights of the Gaussian acceleration pulses are uncertain within $\approx 6\%$ that is determined by poorly defined initial velocities acquired by the erupting structures during the initiation stage. The faster northern core segment underwent the second acceleration episode around

23:59 at a distance of $\approx 8\ R_{\odot}$. Having undergone the acceleration and shape change, the FS expanded with a constant velocity. Its small acceleration around 23:00 might be related to the stretching of its northern part.

The measurements are illustrated by the resized movies in the Electronic Supplementary Material, in which the expansion of the FS (STEREO-A_fs.mpg and AIA_LASCO_fs.mpg) or the fast northern core segment (AIA_LASCO_core.mpg) is compensated for. The CME expansion in the movies is not perfectly self-similar; the core segments to the FS size ratios increase. This character of the CME expansion is indicated by the ratios of the distances in Figure 5a. Note that Grechnev *et al.* (2019) found in a different event indications of a decreasing gap between the FS and core in the CME/ICME expansion. In addition to the color arcs that correspond to our fit, the orange arc represents the fit found by Gopalswamy *et al.* (2015). The orange arc starts to move earlier and closer to the solar-disk center than the erupting prominence and after 21:56 almost coincides with our fit. The comparison demonstrates the accuracy of our fit of the impulsive prominence acceleration.

3.3. Kinematics of the Erupting Filament in the Radial Direction

According to Filippov, Gopalswamy, and Lozhechkin (2001, 2002) and Filippov and Koutchmy (2008), an erupting filament (visible as a prominence above the limb) lifts off along a magnetic surface that is constituted by the neutral lines of the radial magnetic field (B_r) at different heights in the corona. This behavior presumably persists when the filament velocity is not very high. The filament body occupies a wide range of altitudes from the ends up to the top, which touches the neutral line at the maximum height. By finding the height of the neutral line of the radial magnetic field extrapolated into the corona, that corresponds to the filament top at each time, it is possible to evaluate its kinematics in the radial direction in the 3D space.

The magnetic-field extrapolation was kindly made for us by A.A. Kochanov from a synoptic magnetogram using the Potential Field Source Surface (PFSS) model available in the SolarSoft package. We warped each height layer of the radial magnetic component to the orthographic projection on a sphere of a proper radius as viewed at 22:00 on 29 September. Comparing the images of the erupting filament observed by SDO/AIA in 304 Å from 21:02 to 22:00 with neutral lines traced at different heights, we selected the height layers, where a neutral line corresponded to the filament top at each time, as shown in Figure 6. The results are presented in Figure 7a with the diamonds.

After 22:00, the B_r neutral lines do not correspond to the erupting filament, while its acceleration was still strong that does not allow estimating the final filament velocity from these measurements using the method described in Section 3.2. However, it is possible to invoke the kinematical measurements made from the STEREO-A vantage point. From the linear fit of the filament/CME-core kinematics shown in Figure 5 to the measurements in the radial direction we found the scaling factor with an accuracy of 1.3%. The kinematical plots for the filament top in the radial direction are shown in Figure 7 by the solid curves.

With a known kinematics of the filament/prominence in the radial direction, it is possible to estimate its orientation relative to the Sun–Earth line. The triangles in Figure 7a present the distance–time measurements of the filament top made from AIA 304 Å images in the plane of the sky. Using the technique described in the preceding paragraph, we found the scaling coefficient, which is equal to the sine of the angle between the eruption direction and the Sun–Earth line. This angle is 39° that coincides with the orientation of N26 W30 found for the CME apex by Bothmer and Mrotzek (2017), being somewhat larger than the angle of 23° corresponding to the estimate of N15 W17 by Wood *et al.* (2016).

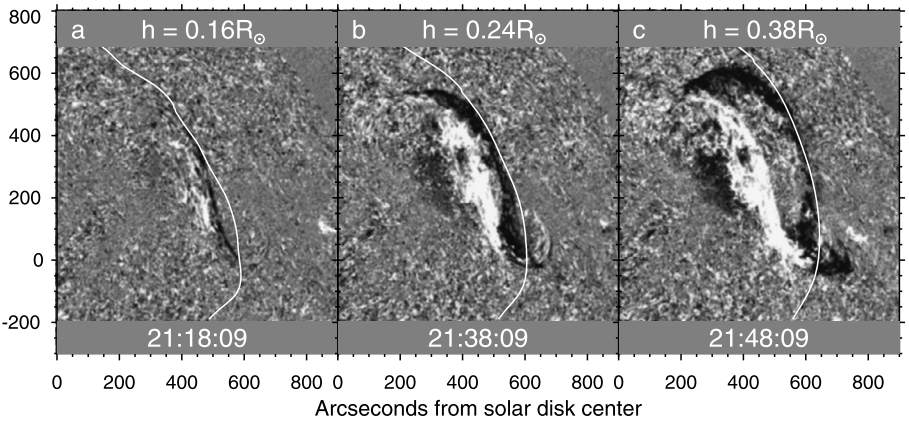

Figure 6 Erupting filament (dark) visible in SDO/AIA 304 Å image ratios along with the white contour of the neutral line of the radial magnetic component B_r extrapolated to different heights in the corona (specified at the top of each panel) to match the top of the filament.

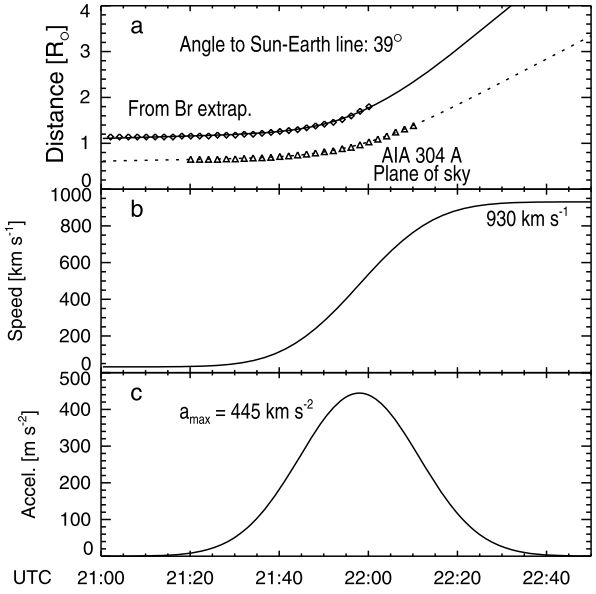

Figure 7 Kinematics of the erupting filament converted to the radial direction. **a**) Distance–time plots. The diamonds represent the heliocentric distances of the filament top in the radial direction estimated from the B_r extrapolation as shown in Figure 6. The triangles represent direct plane-of-the-sky measurements of the filament top from SDO/AIA 304 Å images. The curves represent the analytic fit of the measurements. **b**) Velocity and **c**) acceleration temporal profiles in the radial direction.

It is also possible to estimate the radial velocity of the FS that is the leading edge of the CME body. With a final velocity of the filament top of 930 km s^{-1} (Figure 7b) and a ratio between the final velocities of the middle core segment and FS presented in Figure 5b, we estimate the final radial velocity of the FS to be 1305 ± 50 km s^{-1}. This value is comparable to different estimates of the CME speed of 1398 ± 50 km s^{-1} (Bothmer and Mrotzek, 2017), 1229 km s^{-1} (Wood *et al.*, 2016), 1370 km s^{-1} in the online halo CME catalog of the Coordinated Data Analysis Workshop (CDAW) at cdaw.gsfc.nasa.gov/CME_list/HALO/halo.html, and 1543 km s^{-1} (Gopalswamy *et al.*, 2015).

This section has shown that comparison between the plane-of-the-sky images and extrapolated radial magnetic component offers an opportunity of estimating the radial kinematics

of an erupting filament, including the magnitude of the velocity vector (also termed "deprojected speed" or "space speed") and its tilt to the Sun–Earth line. The results provided by this technique agree with 3D reconstructions that were based on different models. Our usage of observations from three vantage points in the kinematical measurements is not crucial; single-spacecraft observations could be used as well. Besides the top of the erupting filament, it is possible to measure the radial kinematics for any of its distinct features (e.g. the southernmost bending in our case).

4. Shock Wave

4.1. Previous Results and Indications

The high CME velocity suggests the presence of a shock wave ahead it. This indication is confirmed by the Type II emission recorded by the Radio and Plasma Wave Investigation (WAVES: Bougeret *et al.*, 1995) on the Wind spacecraft and by the Radio and Plasma Wave Investigation on the STEREO mission (S/WAVES: Bougeret *et al.*, 2008). Having considered the dynamic radio spectra recorded by the Radio Solar Telescope Network (RSTN: Guidice, 1979; Guidice *et al.*, 1981) and by Wind/WAVES, Gopalswamy *et al.* (2015) stated that the Type II emission started at a frequency of 10 – 13 MHz without a metric component. Relating the Type II onset to the shock formation, the authors estimated it to occur at a heliocentric distance of 2.5 $R_{\odot}$. They assumed that a bow shock was excited by the nose of the CME when it became super-Alfvénic and did not consider any alternative. However, some circumstances need to be specified.

One point of interest is the shock formation time that is invoked, for example, to determine the "accelerator" of SEPs (e.g. Reames, 2009; Grechnev *et al.*, 2017). While a high CME speed indicates the presence of a shock wave ahead of its body, this does not guarantee that the shock wave had appeared not earlier than the CME speed exceeded the Alfvén speed. Different shock-excitation mechanisms do exist (see, e.g., Vršnak and Cliver, 2008). Several case studies of flare-associated eruptions (e.g. Grechnev *et al.*, 2011, 2014, 2015b, 2016, 2017, 2018) concluded that shock waves in all of the events analyzed were initially excited in the impulsive-piston scenario. Here, the 3D impulsive expansion of an erupting structure produces a strong MHD disturbance that has properties of a simple wave, which then steepens into the so-called piston-shock (Vršnak and Cliver, 2008). The formation of a discontinuity is facilitated by a steep falloff of the fast-mode speed away from the wave origin; propagating into environment of a lower fast-mode speed, the MHD disturbance undergoes jamming of its profile and rapidly steepens into the shock (Afanasyev, Uralov, and Grechnev, 2013). The impulsive-piston scenario turns out to be more efficient and forms the shock discontinuity earlier than the bow shock would appear.

The piston-shock kinematics is determined by the trailing piston that spends energy to extrude plasma from the volume that it occupied previously and initially resembles a decelerating gas-dynamic blast wave propagating from a point-like source (Grechnev *et al.*, 2008). The piston-shock deceleration is thus determined by the plasma-density falloff away from the wave origin. If a CME is fast, then later the piston-shock transforms into a bow shock or decays into a weak disturbance otherwise (e.g. Grechnev *et al.*, 2015b, 2016, 2017). The possibility of the initial bow-shock excitation is not excluded for gradually accelerating non-flare-associated CMEs; so far we are aware of the only candidate event reported by Fainshtein and Egorov (2019). To determine if the shock wave in our event was initially excited as a piston-shock or a bow shock, we examine wave manifestations in dynamic radio spectra and images.

4.2. Description of Dynamic Radio Spectra

An associated issue to be clarified is the onset time of the Type II burst. The RSTN radiospectrograph at Kaena point and especially the Culgoora radiospectrograph (Prestage *et al.*, 1994), whose lowest frequency is 18 MHz, reveal a metric burst at frequencies of $\lesssim 36$ MHz during 21:53 – 21:57 that is visible in Figure 8a. We examine the combinations of the STEREO-A/WAVES and Wind/WAVES spectra with the metric Culgoora spectrum and do not consider the STEREO-B spectrum that only shows a few small fragments of Type II bands. To identify Type II signatures in dynamic radio spectra, it is useful to invoke additional indications. We plot over the combined spectra the trajectory expected for an impulsively excited shock wave as done in several studies listed in the preceding section.

The technique uses a power-law coronal-density model $n(x) = n_0(x/h_0)^{-\delta}$ where x is the distance from the wave origin, n_0 is the density at a distance $h_0 = 100$ Mm that is close to the scale height, and δ is the density falloff exponent. Referring to a characteristic point on the dynamic spectrum at time t_1, we specify a frequency and calculate a corresponding distance x_1 from our density model for the plasma frequency and its harmonic(s). Then, adjusting δ and the wave onset time t_0, we calculate the Type II trajectory as $x(t) = x_1[(t - t_0)/(t - t_1)]^{2/(5-\delta)}$ and in sequential attempts endeavor to reach its best fit to all possible Type II signatures in the dynamic spectra. We used the wave onset time $t_0 = 21{:}41 \pm 1.5$ minutes and $\delta = 2.79 \pm 0.05$ for the trajectories calculated for the fundamental (F) and harmonic (H) emissions.

Figures 8a and 8b show an expanded initial part of the combined spectrum. A short metric burst visible in the Culgoora spectrum from 21:53 to 21:57 is a harmonic counterpart to an enhancement around 10 MHz in the Wind/WAVES spectrum. Their visible parts lie on the expected Type II trajectories and have similar shapes that possibly indicate the shock passage through a closed (e.g. loop-like) structure. The decametric enhancement can also be identified in Figure 8f, where it is barely detectable. A group of weak metric Type III bursts (group 1) is detectable within a limited frequency range.

The Wind/WAVES spectrum in Figure 8d and the STEREO-A/WAVES spectrum in Figure 8f, both combined with the Culgoora spectrum (Figures 8c and 8e), show the correspondence of the calculated trajectories to fragmentary Type II signatures, most of which can be categorized as "blobs and bands" according to Cane and Erickson (2005). Besides the overall similarity of the two spectra, differences are present; some features are better visible in Figure 8d and some others in Figure 8f. For example, two short bands denoted "A" are present in Figures 8d and 8f during 22:40 – 22:55 at the second and fourth harmonics. The STEREO-A/WAVES spectrum shows the latter band better. Conversely, harmonic blobs denoted "B" are better visible in the Wind/WAVES spectrum. Also, the Wind/WAVES spectrum clearly shows a band of the fundamental emission denoted "C" from 00:10 to 01:50, to which a weaker harmonic emission corresponds. The STEREO-A/WAVES spectrum only shows two blobs of the fundamental emission in this interval.

Figure 9 presents the Type II emission in the whole interval of its observation. A group of Type III bursts (group 2) is associated with at least three CME bubbles and two to three jets that appeared on 30 September during 16:00 – 20:00 above the east and west limbs (see STEREO-B movies at cdaw.gsfc.nasa.gov/stereo/daily_movies). The slowly drifting portions of these disturbed Type IIIs around 100 kHz trace the shock passage (see, e.g., Pohjolainen, Hori, and Sakurai, 2008). Overall, Type II signatures appear in Figures 8 and 9 with interruptions along the same trajectories down to 70 kHz (harmonic emission) that indicates their common origin due to a single shock wave.

The interplanetary Type II emission can only be narrow-band, if its source is compact, being located in a narrow structure such as a coronal ray (Uralova and Uralov, 1994; Reiner

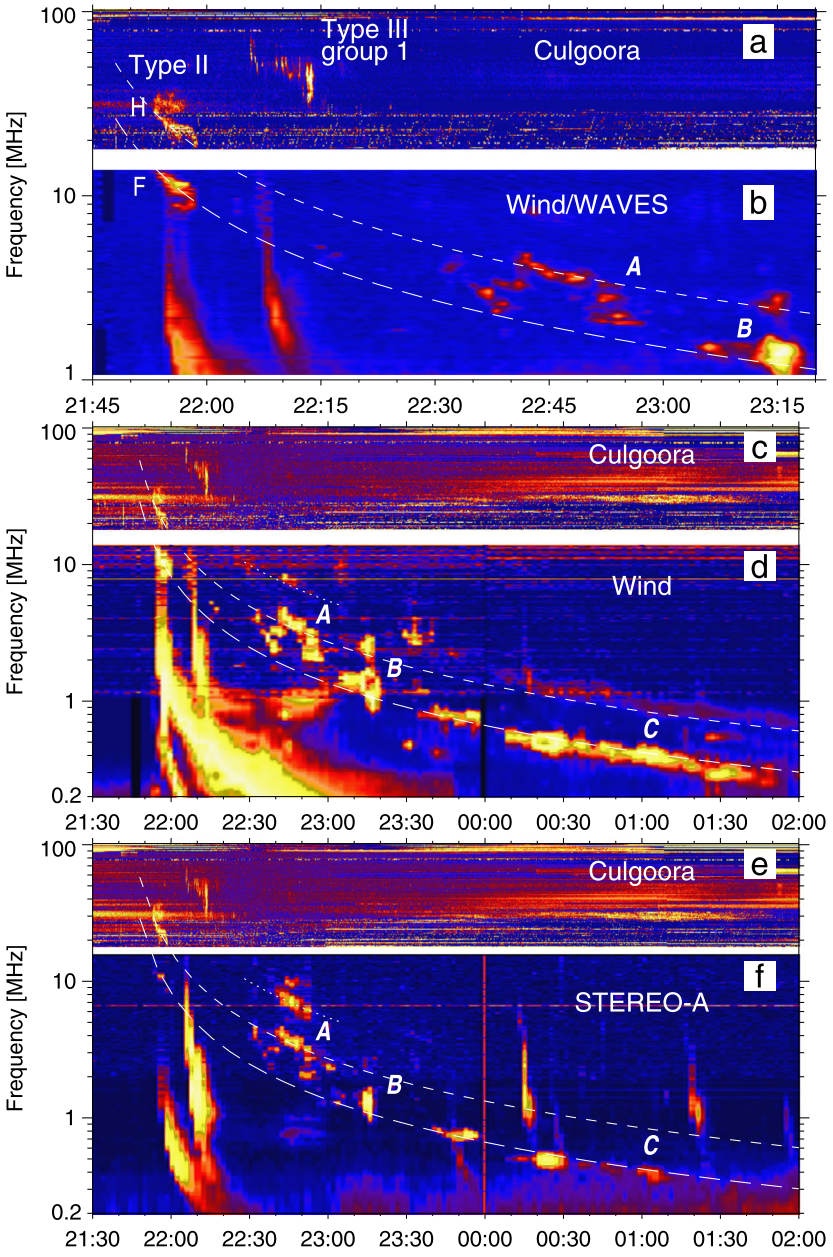

Figure 8 Type II emission recorded by the Culgoora spectrograph (18 – 100 MHz, **a**, **c**, and **e**), Wind/WAVES (**b** and **d**), and STEREO-A/WAVES (**f**). (**a**, **b**) Expanded initial interval. (**d**, **f**) Comparison of the spectra observed from different vantage points of Wind and STEREO-A. Labels "A", "B", and "C" denote harmonic features that appear dissimilar in their spectra. The Wind/WAVES spectra in panels **b** and **d** are displayed in different ways to reveal the features of interest. The white curves of different line styles represent the Type II trajectories calculated for the fundamental emission at the plasma frequency (f_p, long-dashed), at the second harmonic ($2f_p$, short-dashed), and at the fourth harmonic ($4f_p$, dotted).

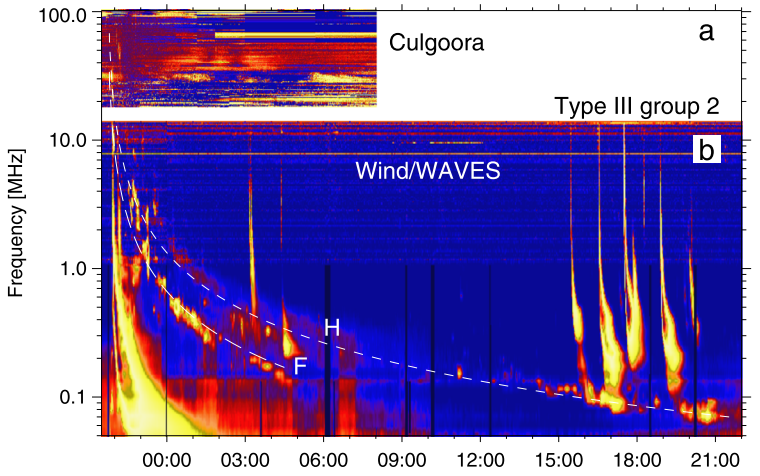

Figure 9 Type II emission recorded by the Culgoora spectrograph (**a**) and Wind/WAVES (**b**) in the whole interval when it was observed.

et al., 2003); otherwise, a drifting continuum is expected from a large shock front crossing a wide range of plasma densities (Knock and Cairns, 2005). On the way to the spectrographs located at different positions in the heliosphere, the emission crosses dense structures, in particular the heliospheric plasma sheet, and may undergo refraction, interference, and/or absorption. A Type II emission from a moving compact source can thus interrupt, reappear, and look different in the spectra obtained at the vantage points of Wind and STEREO (Grechnev *et al.*, 2017).

The correspondence of the calculated trajectories to the Type II signatures from the metric through kilometric range addresses the concern of Cane and Erickson (2005) about an apparent frequency disjoint between a metric Type II burst and interplanetary emission presumably related to the CME shock. In fact, the trajectories correspond to a single shock wave in the whole frequency range down to 70 kHz. To our knowledge, the only similar example was demonstrated previously by Grechnev *et al.* (2017); our case seems to be simpler and clearer.

4.3. Wave Signatures in EUV and Coronagraph Images

As is well known, it is not possible to determine the height of a Type II source from a dynamic spectrum, because n_0 and h_0 may be taken with arbitrary multipliers. Instead, we endeavored to catch wave signatures in EUV and white-light images in Figure 10 using the results obtained in fitting the dynamic spectra. The black-on-white arcs in the figure represent the wave fronts calculated with $t_0 = 21{:}42$ and $\delta = 2.83$. The virtual position of the point-like wave source is close to solar-disk center at $[80'', -150'']$ that takes account of the time required for the wave to propagate from its compact virtual origin to the extended actual driver, i.e. erupting filament. With these parameters, the wave front passed the top of the erupting filament in Figure 10a shortly before the peak of its acceleration (Figure 5c), then passed the shell in Figure 10b and accelerated it. The wave fronts calculated as ellipses with large axes at 60° from the western direction acceptably match the wave traces visible as a halo surrounding the CME body in Figures 10c and 10d. The northern bulge, to which the measurements for the fastest CME-related feature (leading edge) made by Gopalswamy

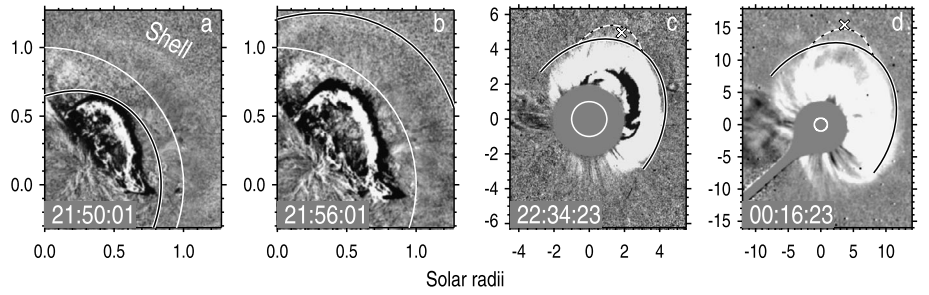

Figure 10 Development and propagation of the wave observed in the AIA 211 Å (**a** and **b**) and LASCO-C2 (**c**) and C3 (**d**) images. The black-on-white solid ellipses represent the wave fronts calculated. The slanted crosses in panels **c** and **d** represent the measurements in the CME catalog. The dashed ellipses in panels **c** and **d** outline the fastest northern bulge measured in the CME catalog. The white-solid circles outline the solar limb.

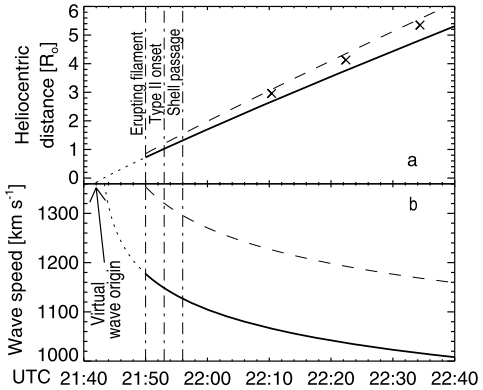

Figure 11 Plane-of-the-sky kinematics of the wave signatures shown in Figure 10. (**a**) Distance–time plot. (**b**) Speed–time plot. The thick-solid curves correspond to the black-on-white solid ellipses in Figure 10. Their thin-dotted initial parts represent the formal expansion of the wave from its virtual origin to the actual driver. The slanted crosses in panel **a** represent the measurements in the CME catalog from LASCO-C2 data. The dashed curves represent the large axes of the dashed ellipses that outline the bulge in Figures 10c and 10d and correspond to the solid curves magnified by a factor of 1.15.

et al. (2015) and presented in the CME catalog (slanted crosses) are related, is outlined in Figures 10c and 10d by dashed elliptic arcs using the same wave kinematics magnified by a factor of 1.15. The central angle of the bulge is 73° from the west that corresponds to the measured position angle of 343° in the CME catalog.

Figure 11 presents the plane-of-the-sky wave kinematics corresponding to Figure 10. The thin-dotted lines represent the formal wave propagation from the virtual point-like source to the actual driver. The vertical dash-dotted lines denote the times when the wave passed the top of the erupting filament in Figure 10a, the shell in Figure 10b, and the onset time of the metric Type II burst at 21:53, when the shock discontinuity was already formed. The decelerating shock-wave kinematics in Figure 11b is different from the velocity–time plots of accelerating erupting structures in Figure 5b that indicates the impulsive piston-shock excitation and not the initial bow-shock excitation, because the kinematics of the piston and wave had been similar in the latter case.

The kinematical plots corresponding to the dashed elliptic arcs that outline the bulge in Figures 10c and 10d are shown in Figure 11 with the dashed lines. The deceleration of the wave and its average speed are consistent with the results of Gopalswamy *et al.* (2015) for the leading edge.

The Type II onset time corresponds to a heliocentric distance of 1.02 $R_\odot$ in the plane of the sky and 1.025 $R_\odot / \sin 39^\circ = 1.62$ $R_\odot$ in the radial direction according to the estimate in Section 3.3, while the orientation of the structure that hosted the Type II source is not known. The two distances put the limits for the position of the Type II source at that time. To specify it, we invoke the Saito model (Saito *et al.*, 1970) that describes the coronal-density distribution above the quiet Sun depending on the heliocentric distance [r] (expressed in solar radii) and latitude [φ]:

$$\frac{n_e(r,\varphi)}{10^8} = \frac{3.09}{r^{16}}(1 - 0.5\sin\varphi) + \frac{1.58}{r^6}(1 - 0.95\sin\varphi) + \frac{0.0251}{r^{2.5}}\left(1 - \sin^{0.5}\varphi\right).$$

As Grechnev *et al.* (2011) showed, the Saito model can be approximated by the power-law density model, in which the argument [x] is the distance from the eruption center that is located above the photosphere ($x \approx (r-1)$ $R_\odot$) and δ depends on the latitude. An increase in the latitude requires a larger δ and lower n_0. For example, $\delta \approx 2.6$ and $n_0 \approx 4.1 \times 10^8$ cm^{-3} for the equatorial Saito model ($\varphi = 0^\circ$). The Saito model at a higher latitude of $\varphi = 60^\circ$ can be approximated with $\delta \approx 2.7$ and $n_0 \approx 4.2 \times 10^7$ cm^{-3}. In our case, $\delta \approx 2.8$ implies that the latitude might possibly be higher.

Calculations from the Saito model show that the starting frequency of the fundamental emission at about 13 MHz in Figure 8d corresponds to the largest possible heliocentric distance of 1.62 $R_\odot$ with a latitude of 55°. For a higher latitude, the distance corresponding to 13 MHz decreases, while the difference between the power-law model with $\delta = 2.79$ and Saito model increases from the initial ±33% to ±54% at $\varphi = 75^\circ$, where $r = 1.43$, and then becomes unacceptable.

Thus, the probable heliocentric distance of the Type II source at its onset ranges from 1.43 $R_\odot$ for its location at a far flank of the shock up to 1.62 $R_\odot$, if it was located exactly above the erupting-filament top. The association with a streamer expected for a Type II source seems to favor its flank location. Deflections of streamers by a wave are really visible northerly from the CME in Figure 3c and in the running-difference STEREO movies (cdaw.gsfc.nasa.gov/stereo/daily_movies/2013/09/29/) starting at 21:55. The range estimated for the latitudes of 55° – 75° roughly corresponds to the orientations of the wave fronts in the plane of the sky presented in Figure 10.

Our estimate of the heliocentric distance of ≤ 1.62 $R_\odot$ for the Type II source at its onset is considerably lower than the shock formation distance 2.5 $R_\odot$ estimated by Gopalswamy *et al.* (2015). We do not associate the two distances with each other. In the scenario outlined in Section 4.1, a Type II burst starts when a streamer is reached by the shock that is already formed. The height of the Type II source is determined by the geometry of the collision and the distance between the streamer and wave origin. The shape of the shock front is most likely close to an ellipsoid (e.g. Grechnev *et al.*, 2011; Kwon, Zhang, and Olmedo, 2014; Kwon, Zhang, and Vourlidas, 2015; Rouillard *et al.*, 2016) that extends over a wide range of altitudes down to the solar surface. It is therefore difficult to assign a certain meaning to the shock formation height.

The overall shock-wave evolution in this event seems to be mainly the same as in flare-associated events. Most likely, the wave was initially excited impulsively by the erupting filament as a piston-shock and transformed later to the bow-shock regime at several solar radii, where the difference between their kinematics diminished (Grechnev *et al.*, 2017). The

shock wave seems to have appeared earlier and closer to the solar surface than Gopalswamy *et al.* (2015) and Cliver *et al.* (2019) assumed. This circumstance has implications to the properties of the SEP event, whose origin in this and similar non-flare-associated events was probably related to the shock wave alone. They are discussed in Section 6.3.

5. Magnetic Flux Involved in the Eruption

5.1. Reconnection Flux Issue

Magnetic reconnection is considered as a key process responsible for the flux-rope formation and flare development (e.g. Inhester, Birn, and Hesse, 1992; Longcope and Beveridge, 2007). The correspondence has been established for flare-associated events between the magnetic-flux reconnection rate and hard X-ray (HXR) or microwave emission (e.g. Miklenic, Veronig, and Vršnak, 2009), between the HXR emission and CME acceleration (e.g. Zhang *et al.*, 2001; Temmer *et al.*, 2008, 2010; Grechnev *et al.*, 2016), between the total reconnected flux, on the one hand, and CME velocity (e.g. Qiu and Yurchyshyn, 2005) and magnetic flux in an ICME (e.g. Qiu *et al.*, 2007), on the other hand.

However, Kahler *et al.* (2017) have not found any correlation between the CME speed and reconnected flux computed in 126 flares by referring to the ribbons visible in SDO/AIA 1600 Å images (their Figure 4). Cliver *et al.* (2019) concluded that the total reconnection flux computed by referring to SDO/AIA 304 Å images was low in the Sep29 event that produced a fast CME. The disagreement between the conclusions of these two studies and the results listed in the preceding paragraph needs clarification.

The magnetic-flux change rate is computed by considering the expansion of flare ribbons (e.g. in the Hα line or in 1600 Å) over a magnetogram (Fletcher and Hudson, 2001; Qiu *et al.*, 2007; Miklenic, Veronig, and Vršnak, 2009; Kahler *et al.*, 2017; Cliver *et al.*, 2019). Its cumulative sum gives the temporal profile of the reconnected flux, whose maximum is total reconnected flux. It can also be estimated from the computation of the total unsigned magnetic flux covered by a coronal arcade, as proposed by Chertok *et al.* (2013) and refined and modified by Gopalswamy *et al.* (2017). The results of the two approaches are expected to be the same, because the ribbons map out the footpoints of the arcade loops (e.g. Fletcher and Hudson, 2001) and the reconnected magnetic flux does not depend on the spectral domain used to reveal it. The difference between the results may be related to the accuracy and sensitivity of the methods.

In this section we firstly compare the magnetic-flux change rate computed by Cliver *et al.* (2019) with the acceleration temporal profile measured in Section 3.2 and then estimate the total reconnected flux using the method of Chertok, Grechnev, and Abunin (2017). In this way, we endeavor to find the reasons why magnetic fluxes could be somewhat underestimated by Chertok *et al.* (2013, 2015) for non-active-region eruptions, as mentioned in Section 1.

5.2. Measurements of Reconnected Flux

Figure 12 compares the acceleration temporal profile that we measured for the fast northern segment of the prominence/CME core with the magnetic-flux reconnection rate (also termed the ribbon flux) measured by Cliver *et al.* (2019). The acceleration profile from Figure 5c was converted to the radial direction that does not affect its shape. Figure 12 shows the following.

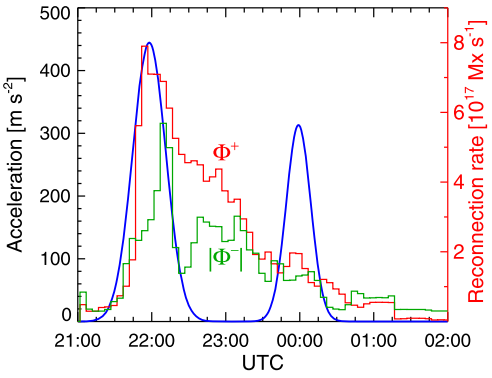

Figure 12 Comparison of the acceleration profile measured for the northern segment of the prominence/CME core (blue curve, same as in Figure 5c) converted to the radial direction with the magnetic-flux reconnection rate adapted from Cliver *et al.* (2019) (histogram-like lines: red positive, green inverted negative).

The reconnection rates measured for the positive flux Φ^+ and the absolute value of the negative flux $|\Phi^-|$ are rather similar to each other, but not identical that is typical of such measurements. Underestimation is possible because of incomplete coverage of the ribbons by the region of the analysis or incomplete detection of the ribbon brightenings. Overestimation may be caused by the presence of low closed loops that do not participate in reconnection, while their footpoints are shown by a magnetogram. More reasons for the difference were discussed by Fletcher and Hudson (2001). Each of the Φ^+ and $|\Phi^-|$ temporal profiles thus represent an approximation for the reconnection rate, and their distinction may be attributed to measurement errors.

The first acceleration peak is close to the peaks in the reconnection rates measured at each of the ribbons. An uncertain counterpart to the second acceleration peak (that occurred around 8 $R_\odot$) is conjectured in the Φ^+ temporal profile. A clear enhancement around 23:00 in $|\Phi^-|$ that is less conspicuous in Φ^+ corresponds to a minor acceleration of the frontal structure in Figure 5c.

The correspondence between the first acceleration peak and the maximum reconnection rate along with possible associations between other features in the temporal profiles in Figure 12 indicate that the Sep29 eruption was governed by reconnection processes, like flare-associated eruptions (e.g. Vršnak, 2008, 2016). Hence, although this event was non-flare-associated (excluding the compact thermal X-ray emission addressed by Holman and Foord, 2015), the CME speed and ICME parameters should be determined by the total reconnected flux. We therefore focus on its estimation. Both the positive reconnected flux $\phi^+_{\rm rec}$ and the absolute value of the negative flux $|\phi^-_{\rm rec}|$ are expected to be equal to the halved total unsigned flux measured, $\phi_{\rm rec} = \Phi_{\rm tu}/2$ (Gopalswamy *et al.*, 2017). Most likely, a minor contribution from the magnetic flux in dimmed regions should not be considered (Qiu *et al.*, 2007).

Cliver *et al.* (2019) measured the total unsigned magnetic flux of $\Phi_{\rm tu} = 2\phi_{\rm rec} = 6.4 \times 10^{21}$ Mx. Using the method and software developed by Chertok, Grechnev, and Abunin (2017), we obtained a close estimate of $\Phi_{\rm tu} = 5.5 \times 10^{21}$ Mx. In this method, the magnetic flux is measured within the contour of an arcade observed in EUV close to the peak time of the SXR emission. The contour of the arcade is identified in a difference image at the 5% level of the brightness increase relative to a pre-eruption image.

We found that with a threshold of 5% significant parts of the arcade are not detected in this event. Also, the measurement near the SXR peak time might be insufficient for non-active-region eruptions that last much longer than flare-associated events. In our event, the maximum of the SXR emission at 23:40 was followed by an additional peak 20 minutes later and then by a long-lasting decay visible in Figures 2a and 2b. As the arcade developed, some

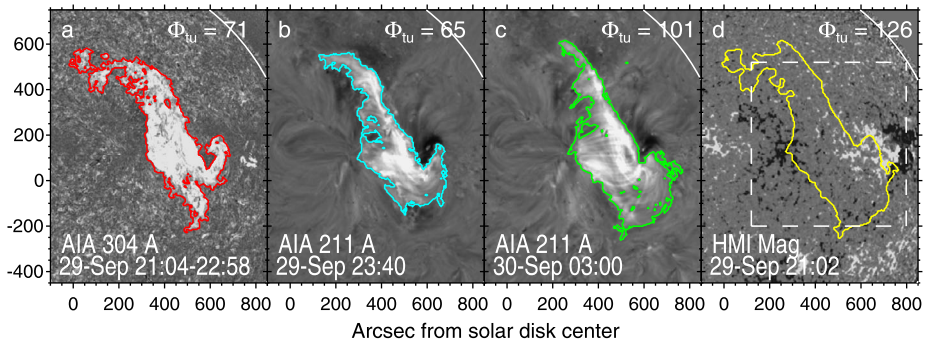

Figure 13 Total unsigned magnetic flux measured within the arcade, whose color contours were identified: (**a**) from AIA 304 Å images, (**b**) from AIA 211 Å image near the maximum of the SXR flux, (**c**) from AIA 211 Å image in a late decay stage. (**d**) The yellow contour of the arcade combining the areas in panels **a**–**c** overlaid on the line-of-sight SDO/HMI magnetogram. The dashed frame denotes the region where Cliver *et al.* (2019) measured the ribbon flux. The total unsigned magnetic flux Φ_{tu} measured within the arcade contour is presented at the top of each panel in units of 10^{20} Mx.

of its parts faded before the appearance of the others that resulted in its incomplete detection from a single image. We reduced the arcade-detection threshold to 1% and considered both the arcade and ribbons at different times, as shown in Figure 13.

The image in Figure 13a was computed as a maximum over the ratios of AIA 304 Å images observed from 21:04 to 22:58 to a pre-event image obtained at 21:02. The ribbon contours were identified at a brightness increase factor of 1.6. This image is similar to some extent to what Cliver *et al.* (2019) considered. The region of their analysis (white-dashed frame in Figure 13d) did not include the northeasternmost portion, where a brightening is also visible in AIA 131 Å images from 22:15 to 23:15 (see, e.g., sdo.gsfc.nasa.gov/data/aiahmi/).

Figures 13b and 13c show the AIA 211 Å difference images overlaid by the contours of the arcade obtained with a brightness threshold of 1% at the SXR peak time and late in the decay stage, respectively. The magnetic flux estimated using the image in Figure 13b practically coincides with the estimate by Cliver *et al.* (2019) that confirms the equivalence of the two methods and justifies the decrease of the brightness threshold. In Figure 13c, the southern and eastern parts of the arcade broadened, while the northeastern edge faded. These changes increased the estimated magnetic flux by 55%; the differences between the values in Figures 13a and 13b and the estimate by Cliver *et al.* (2019) are within 11%.

The yellow contour in Figure 13d combines the three areas occupied by the ribbons and the arcade in Figures 13a–13c. The total area is 1.4×10^{21} cm^2. The total magnetic flux within the whole area is $\Phi_{tu} = 2\phi_{rec} = 12.6 \times 10^{21}$ Mx that is about twice higher than the estimates obtained by Cliver *et al.* (2019) and using the method by Chertok, Grechnev, and Abunin (2017). The compensation for the projection shrinkage increased the estimate by 24%. To determine how realistic our estimate is, we invoke additional indications.

5.3. Reconnection Flux and CME Speed

Chen and Krall (2003) showed that the ultimate CME speed is determined by the total amount of poloidal flux or magnetic energy injected into an erupting flux rope. According to Qiu *et al.* (2007) and Miklenic, Veronig, and Vršnak (2009), the main contribution to the poloidal flux is supplied by reconnection operating during the eruption and a corresponding flare, if it is present. A direct dependence of the CME speed on the reconnected

magnetic flux is thus expected that was confirmed observationally (e.g. Qiu and Yurchyshyn, 2005) and demonstrated theoretically (Vršnak, 2008, 2016). Flare-associated and non-flare-associated eruptions seem to be governed by basically the same processes (e.g. Chertok, Grechnev, and Uralov, 2009). These circumstances lead to a general dependence of the CME speed on the reconnected flux irrespective to the presence or absence of a conspicuous flare. This dependence has really been established by Gopalswamy *et al.* (2017) and elaborated by Pal *et al.* (2018). According to the statistical pattern found in the latter study, the deprojected CME speed $V_{\rm CME}$ is related to the reconnected flux $\phi_{\rm rec}$ as

$$V_{\rm CME} = 355\left(\phi_{\rm rec}/10^{21}\right)^{0.69}\ {\rm km\,s^{-1}}, \tag{1}$$

where $\phi_{\rm rec}$ is measured in Mx. We have modified hereafter the formulas presented by the authors to avoid confusions that the usage of different units may cause.

With a deprojected speed of our CME from 1229 to 1543 km s^{-1} (Section 3.3), the total reconnected flux is expected to be $\phi_{\rm rec} \approx (6.0-8.4) \times 10^{21}$ Mx and the total unsigned magnetic flux $\Phi_{\rm tu} \approx (12.0-16.8) \times 10^{21}$ Mx that corresponds to our estimate in the preceding section. The magnetic flux that would be consistent with the parameters of space-weather disturbances is discussed in Section 6.2.

On the other hand, the reconnection flux of $\phi_{\rm rec} = 6.4/2 \times 10^{21}$ Mx measured by Cliver *et al.* (2019) corresponds to a lower CME speed of 792 km s^{-1} expected from Equation 1. Further, to compare the reconnection flux in the Sep29 event with the events that Kahler *et al.* (2017) analyzed by referring to the ribbons identified in 1600 Å, Cliver *et al.* (2019) estimated it in this way to be $\Phi_{\rm tu} \leq 10^{21}$ Mx. The authors concluded that the reconnection flux was low in this event; they also assumed that the shock wave was driven by a fast CME.

It is difficult to agree with these statements, because: i) the reconnection flux does not depend on the spectral domain used to evaluate it, while flare-like manifestations in non-flare-associated (non-active-region) events are weak, if any; ii) the CME speed expected from Equation 1 with $\phi_{\rm rec} = 1/2 \times 10^{21}$ Mx is 220 km s^{-1} that is much lower than the actual speed. Although Equation 1 applies statistically, a CME with a comparable speed cannot drive a bow shock.

Kahler *et al.* (2017) and Cliver *et al.* (2019) related the reconnection flux only to the flare size that is low in non-active-region events. The reconnection rate and total reconnected flux also determine the acceleration and final speed of a CME and are not expected to be low, if the CME is fast. On the other hand, the SXR flux is proportional to the emission measure ${\rm EM} = n^2 V$ with $n = N/V$ being a number density of emitting electrons (ions), whose total number is N. With a given number N of particles of plasma heated to equal temperatures in different arcades, ${\rm EM} \propto 1/V$ that strongly reduces the GOES importance of non-active-region arcades that occupy huge areas. Thus, the reconnection flux is not necessarily low, if a flare is weak, being probably related more directly to the CME kinematics (excluding confined flares) than to the flare size.

A question remains about the CME speeds uncorrelated with reconnection fluxes found by Kahler *et al.* (2017), contrary to the results of Qiu and Yurchyshyn (2005), Gopalswamy *et al.* (2017), and Pal *et al.* (2018). An inverse dependence of the Sun–Earth transit time on the magnetic flux found by Chertok *et al.* (2013) also implies the correlation between the latter and the CME speed. Incomplete detection of flare ribbons in 1600 Å images may account for disaccord.

Section 5 has shown that the reconnected flux evaluated in this non-active-region event with the criteria used for flare-associated eruptions may be considerably underestimated. Using the method of Chertok *et al.* (2013) and Chertok, Grechnev, and Abunin (2017), we

found the underestimation factor of up to about two. It may be higher, if chromospheric emissions are only considered. Defining the arcade region within a polygon in the method of Gopalswamy *et al.* (2017) seems to overcome the problem, but overestimation becomes possible. A universal method that would be free of disadvantages is not obvious so far.

6. Space Weather Disturbances

A prompt consequence of the solar eruptive event was a big proton enhancement in the Earth orbit. Then the arrival of an interplanetary disturbance that developed from the CME caused a Forbush decrease and moderate geomagnetic storm (Section 2 and Figure 2). Wood *et al.* (2016) stated that the shock hit Earth and did not exclude the ICME hitting Earth as well. Bothmer and Mrotzek (2017) showed that the ICME really hit Earth. Here we consider the ICME and compare the parameters observed with expectations. Then we discuss the proton enhancement and possible implications of our results to solar proton events.

6.1. ICME

The interplanetary disturbance was measured in situ by the instruments of the Advanced Composition Explorer (ACE: Stone *et al.*, 1998) whose data are available at the ACE Science Center (www.srl.caltech.edu/ACE/ASC/index.html). We use the data from the Solar Wind Electron Proton Alpha Monitor (SWEPAM: McComas *et al.*, 1998) merged with the Solar Wind Ion Composition Spectrometer (SWICS: Gloeckler *et al.*, 1992) to fill the gaps in the SWEPAM observations, and the data from the Magnetic Fields Experiment (MAG: Smith *et al.*, 1998).

Figure 14 presents the variations of the solar-wind parameters measured by ACE several days around the arrival of the ICME. Our identification of the shock arrival time and ICME boundaries corresponds to the results of Bothmer and Mrotzek (2017), who additionally considered the magnetic-field azimuthal angle which we do not show. The shock arrival (dotted line) is marked by the jumps in the proton velocity, density, temperature, and magnetic-field magnitude. The passage of the magnetic cloud (MC) within the dashed lines is indicated by the low density, temperature, plasma beta, and gradual magnetic-field variations.

The shock arrival was preceded by reduced beta values and relatively systematic behavior of the magnetic field, whose components became fluctuating on 1 October. The cosmic-ray level in Figure 2d also decreased well before 2 October. These facts indicate the passage of a different slow ICME, whose source is not known. The ACE data shown in Figure 14 suggest that the eastern part of the ICME produced on 29 September temporally extruded the slow ICME from 23:30 on 2 October until 19:00 on 3 October, when the passage of the slow ICME resumed. This transition is marked in Figure 2 by the changes in the > 10 MeV proton flux, cosmic-ray level, and the Dst index.

The variations of the magnetic components in the MC correspond to the expectations inferred in Section 2 from solar observations for a left-handed flux rope with an axis directed nearly parallel to the solar rotation axis (the schemes in Figures 1d and 1e). A short temporal interval preceding the MC, where $10^{-2} < \beta < 10^{-1}$, indicates an interaction between our ICME and slow ICME. The B_x component was antiparallel in our ICME and in the slow CME, suggesting reconnection between them that seems to be a quite common phenomenon (Démoulin, 2010). An expected outcome is a decrease of the poloidal flux in the ICME.

Based on the conclusion of Qiu *et al.* (2007) that the main amount of the poloidal flux in an ICME is supplied by reconnection, it is possible to estimate the reconnected flux. With

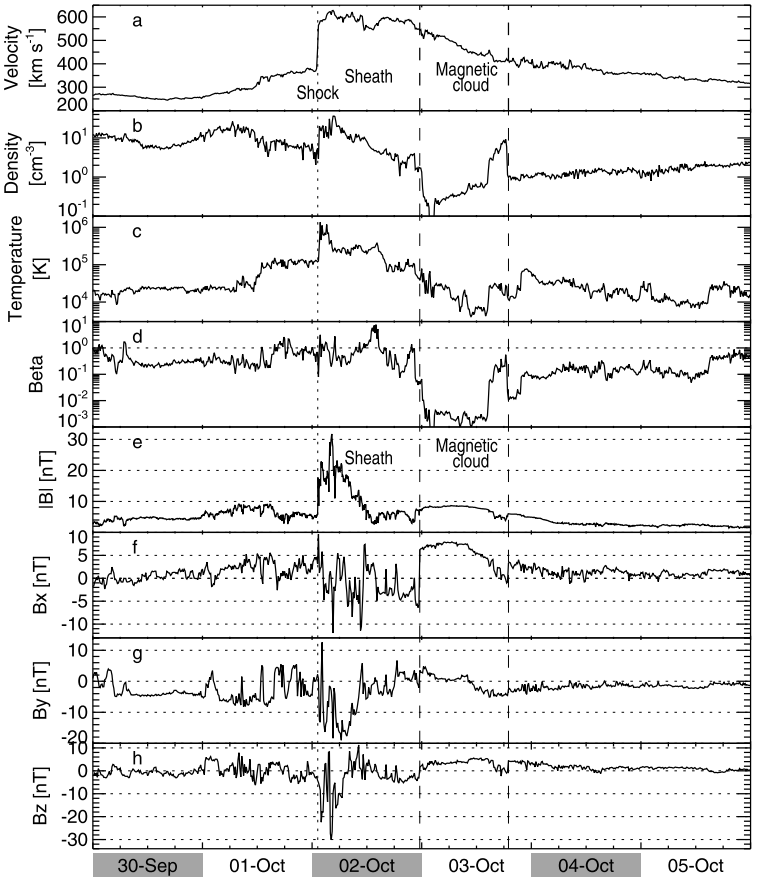

Figure 14 Interplanetary transient measured in situ on ACE: velocity (**a**), proton density (**b**), proton temperature (**c**), plasma beta (**d**), the magnitude of the magnetic-field vector (**e**), and its components (**f**, **g**, and **h**) in the GSE system. The dotted vertical line marks the shock arrival. The leading edge of the magnetic cloud and its presumable trailing edge are denoted by the dashed vertical line. The day numbers are centered at the noon of each date.

a huge initial size of the erupted prominence, the CME expansion was most likely radial from the beginning, so that the expansion factor to the ACE position at the L1 Lagrangian point was $k_{\rm exp} \approx 213$. The total area of the arcade estimated in Section 5.2 was $A_{\rm arc} \approx 1.4 \times 10^{21}$ cm^2. With a maximum magnetic-field strength in the MC of $B_{\rm max} \approx 8.5$ nT, the total unsigned magnetic flux is $\Phi_{\rm tu} = 2\phi_{\rm rec} \approx 8.5 \times 10^{-5} \times k_{\rm exp}^2 \times A_{\rm arc} \approx 5.4 \times 10^{21}$ Mx. This simple estimation ignores several factors and may lead to an underestimated result, especially because of the unknown decrease in the magnetic flux due to reconnection in the interplanetary space. Nevertheless, this estimate certainly exceeds the value of 1×10^{21} Mx considered by Cliver *et al.* (2019).

The strongest negative B_z occurred in the sheath soon after the shock arrival that accounted for the prompt occurrence of the minimum Dst $= -72$ nT at 08:00 on 2 October (Figure 2e). Sheath regions, where B_z is unlikely predictable, are often responsible for geomagnetic storms (Yermolaev *et al.*, 2012).

6.2. Expected and Observed Parameters of the Disturbance

From the analysis of intense non-recurrent geomagnetic storms with a minimum Dst < -100 nT in Solar Cycle 23, whose more or less reliably identified solar sources were located within 45° from the solar-disk center, Chertok *et al.* (2013, 2015) obtained statistical relations between the erupted magnetic flux and some parameters of a geospace disturbance. These empirical formulas characterize the expected temporal intervals between the peak of an associated SXR emission and the onset ($\Delta T_{\rm onset}$) and peak ($\Delta T_{\rm peak}$) of a geomagnetic storm, the depth of the Forbush decrease ($A_{\rm F}$), and the storm intensity in terms of the Dst and ap indices. Chertok, Grechnev, and Abunin (2017) updated these relations for the usage of SDO data in Solar Cycle 24 considering the fact that magnetic fields measured by SDO/HMI were weaker by a factor of 1.4 than the SOHO's Michelson Doppler Imager (MDI: Scherrer *et al.*, 1995) showed (Liu *et al.*, 2012). These relations expressed in terms of the reconnected flux (in Mx) are as follows:

$$\begin{aligned}
\Delta T_{\rm onset}\ [\text{hours}] &= 98/\left[1+0.00616\left(2\phi_{\rm rec}/10^{20}\right)\right],\\
\Delta T_{\rm peak}\ [\text{hours}] &= 118/\left[1+0.0056\left(2\phi_{\rm rec}/10^{20}\right)\right],\\
A_{\rm F}\ [\%] &= -0.3+0.042\left(2\phi_{\rm rec}/10^{20}\right),\\
\text{Dst}\ [\text{nT}] &= 30-15.4\left[\left(2\phi_{\rm rec}/10^{20}\right)+3.8\right]^{1/2},\\
\text{ap}\ [2\text{nT}] &= 1.12\left(2\phi_{\rm rec}/10^{20}\right).
\end{aligned} \tag{2}$$

These parameters for the disturbance caused by the Sep29 event were $\Delta T_{\rm onset} \approx 50$ hours, $\Delta T_{\rm peak} \approx 56$ hours, $A_{\rm F} \approx 4.6\%$, Dst $= -72$ nT, and ap $= 179$. We assess the closeness of a set of n parameters $p_i^{\rm exp}(\phi_{\rm rec})$ expected from Equations 2 for a given reconnected flux $\phi_{\rm rec}$ (or $\Phi_{\rm tu}$) to the values actually observed $p_i^{\rm obs}$ using a relative deviation $q(\phi_{\rm rec})$ defined as

$$q(\phi_{\rm rec}) = \sqrt{1/n\sum_{i=1}^{n}\left[p_i^{\rm obs}-p_i^{\rm exp}(\phi_{\rm rec})\right]^2/\left(p_i^{\rm obs}\right)^2}. \tag{3}$$

We use the relative deviation for an arbitrary number of parameters, including the case of a single parameter. Figure 15 presents the dependencies of the deviations of $p^{\rm exp}$ from the actual parameters in our event on the total unsigned magnetic flux $\Phi_{\rm tu} = 2\phi_{\rm rec}$. The minimums indicate its probable values.

We combined the parameters that describe similar characteristics, i.e. $\Delta T_{\rm onset}$ and $\Delta T_{\rm peak}$ in Figure 15a and indices Dst and ap in Figure 15b (dotted curves). Only Dst indicates a lower magnetic flux that is not surprising; Equations 2 were obtained for intense geomagnetic storms, where strong negative B_z was probably long-lasting, unlike our ICME with a short-term negative B_z in the sheath (Figure 14h). On the other hand, the transit times, that are tightly related to the CME/ICME speed of our main interest, indicate a higher magnetic flux. The combined assessment leads to $\Phi_{\rm tu} = 2\phi_{\rm rec} \approx 99 \times 10^{20}$ Mx (94×10^{20} Mx with each parameter assessed individually). The value of 126×10^{20} Mx obtained in Section 5.2 does not contradict the plots in Figure 15. The two estimates bound a probable range of the magnetic flux. The distribution of geoeffective events vs. magnetic flux is presented and discussed in the next section.

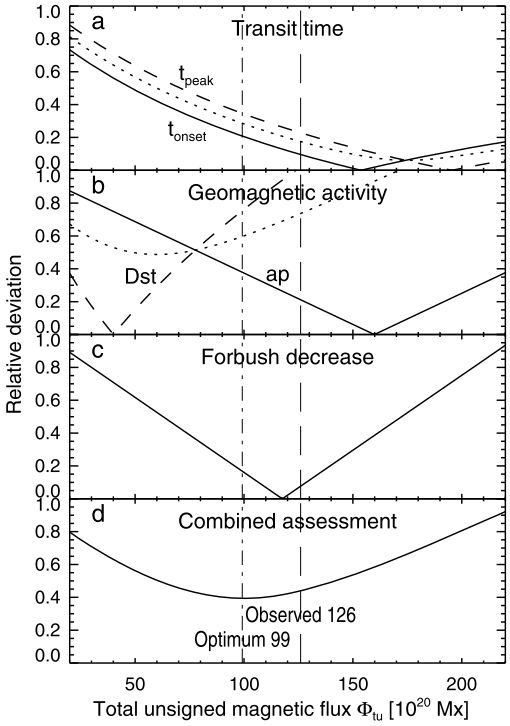

Figure 15 Comparison of actual parameters of the geospace disturbance with expectations according to Chertok, Grechnev, and Abunin (2017) based on the total unsigned magnetic flux involved in the eruption. The dotted curves in panels **a** and **b** combine similar parameters. The vertical dash-dotted line denotes the magnetic flux corresponding to the minimum deviation. The vertical dashed line marks the magnetic flux actually measured.

6.3. Proton Enhancement and Implications

As mentioned in Section 1, consensus has not been reached so far about the roles of flare processes and shock waves in the acceleration of SEP protons. Non-flare-associated SEP events deserve special attention, being a rare situation when a single source of accelerated protons appears to be certain. Manifestations of flare-accelerated electrons are usually manifold, particularly in non-thermal bursts observed in hard X-rays, microwaves, and as metric Type IIIs. However, no microwave burst was detected in this event. Holman and Foord (2015) have not found any non-thermal component in the spectrum of its X-ray emission. Weak metric Type IIIs (group 1 in Figure 8a) are barely detectable in a rather narrow frequency range. While the presence of flare-accelerated electrons is questionable in this event, the near-Earth proton enhancement that it produced was large. These facts indicate that the shock wave alone accelerated SEP protons in this case.

The SEP29 event produced a near-Earth proton enhancement up to $J_{10} \approx 180$ pfu in the > 10 MeV integral proton channel that started on 29 September at 23:50 (Gopalswamy *et al.*, 2015) and up to $J_{100} \approx 0.14$ pfu in the > 100 MeV channel that started somewhat later than the > 10 MeV flux (Figure 2c). The delay seems to correspond to what is expected for the shock-acceleration, where some time is required to accelerate protons to higher energies. The rise of the higher-energy proton flux had a considerable duration, although the source region was close to a well-connected position. This feature also seems to agree with the shock-acceleration that may continue at considerable distances from the Sun, thus augmenting the proton flux. Three different non-flare-associated SEP events addressed by Gopalswamy *et al.* (2015) exhibited similar behaviors. After the maximum of the SEP event, the decrease in the proton flux from early 2 October until about 19:00 on 3 October

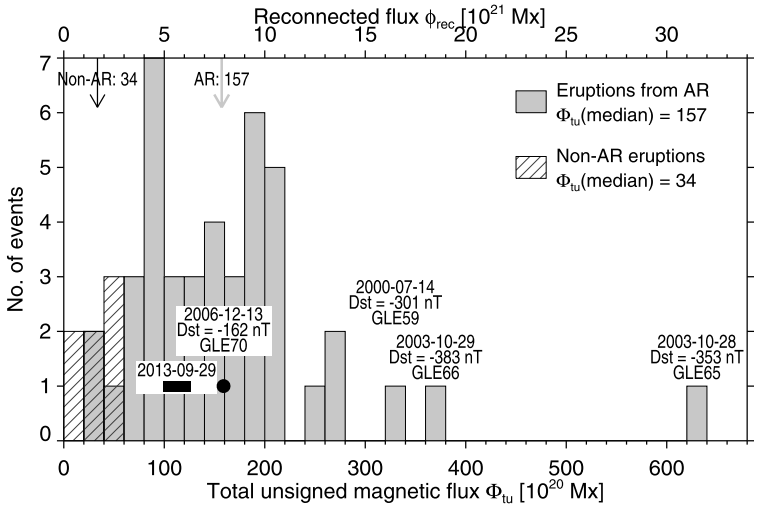

Figure 16 Distribution of events responsible for intense geomagnetic storms in Solar Cycle 23 vs. erupted magnetic flux in units of 10^{20} Mx according to Chertok *et al.* (2013). Magnetic fluxes measured from SOHO/MDI magnetograms were reduced by a factor of 1.4 to match SDO/HMI data. The upper horizontal axis presents the reconnected flux $\phi_{rec} = \Phi_{tu}/2$ in units of 10^{21} Mx for convenience. The thick-black bar shows a probable range for the reconnected flux in the Sep29 event. Four extreme events that caused GLEs are specified.

was caused by the passage of the fast ICME produced in the Sep29 event (Section 6.1) that partly screened the Earth environment from both solar protons and non-solar cosmic rays (Figure 2d).

To characterize the slope of the proton spectrum between 10 and 100 MeV, we use a parameter $\delta_p = \log_{10}(J_{10}/J_{100})$ that is calculated from different-energy peak fluxes occurring at different times, thus attempting to compensate for the velocity dispersion. The $\delta_p \approx 3.1$ value in this SEP event indicates a considerably softer proton spectrum in the 10 – 100 MeV energy range than in most SEP events (Chertok, Grechnev, and Meshalkina, 2009; Grechnev *et al.*, 2013, 2015a).

Now we compare the magnetic flux estimated for our event with the events that caused intense geomagnetic storms in Solar Cycle 23 using the measurements from Chertok *et al.* (2013). Their set contains large proton events, including ground-level enhancements of cosmic-ray intensity (GLEs), for which GeV-energy protons are responsible. Figure 16 shows the event distribution vs. erupted magnetic flux converted to the SDO/HMI calibration. The shaded histogram represents flare-associated active-region events; the hatched histogram represents non-flare-associated events. The magnetic flux may be overestimated for flare-associated events, because Chertok *et al.* (2013) included dimming regions, while for non-flare-associated events it is most likely underestimated, as discussed in preceding sections. Three extreme events with a GOES importance of $\geq$ X5.7 that caused geomagnetic superstorms and GLEs are specified as well as the SOL2006-12-13 X3.4 event with $\Phi_{tu} \approx 159 \times 10^{20}$ Mx responsible for GLE70 (black disk). The vertical arrows mark the median value (a proxy for the most-frequent value) of the magnetic flux for each of the two categories of events. The thick-black bar represents the Sep29 event.

The selection of geoeffective eruptions filters out numerous weaker events and many moderate to major events, whose geomagnetic impact did not exceed -100 nT in terms of

the Dst index or the angular distance of the source region from the solar-disk center exceeded 45°. Nevertheless, the set of 50 geoeffective events shown in Figure 16 seems to be sufficient to draw some conclusions.

Firstly, while the GOES importance of flare-associated events ranges from B7.5 to X17.2, i.e. by a factor of ≈ 2300 (Chertok *et al.*, 2013), the maximum to minimum ratio of their magnetic fluxes is as small as ≈ 20. Considering that the geomagnetic impact directly depends on the ICME speed (with $B_z < 0$), the CMEs in these events are expected to be sufficiently fast. Indeed, the range of CME speeds expected from Equation 1 is $20^{0.69} \approx 8$. Hence, Figure 16 may roughly be considered as a proxy for the CME speed distribution that is consistent with a suggestion that the reconnection flux primarily determines the CME speed (Section 5.3). The eruption duration is significant for the reconnection rate. With a reconnection-flux ratio for the SOL2003-10-28 and SOL2013-09-29 events of about five, the ratio of their maximum reconnection rates is about 80 (Miklenic, Veronig, and Vršnak, 2009; Cliver *et al.*, 2019) that seems to characterize the accelerations of the eruptions, probably also nonlinearly.

The magnetic flux in the Sep29 event falls within the range of flare-associated eruptions, being comparable with their typical value of 157×10^{20} Mx and particularly with the SOL2006-12-13 GLE70 event. The deprojected CME speed estimated in the online halo CME catalog for the latter event was 2184 km s^{-1} that is not far from the expectation based on the CME speed in our event and the reconnected-flux ratio. Thus, i) our event possessed a considerable reconnection flux, being not an outlier in the proton intensity vs. reconnection-flux distribution (Figure 5 in Cliver *et al.*, 2019), and ii) the CME speed alone does not determine the proton outcome of an event entirely. Gopalswamy *et al.* (2015) and other authors consider the shock formation height to be important.

As several recent observational studies listed in Section 4.1 concluded, shock waves develop in the low corona during the early formation of CMEs that also was most likely the case in our event. The conclusion about the low-corona shock formation may be helpful for studies of particle acceleration by shock waves, decreasing the allowed height where it can occur and thus extending the acceptable range of plasma parameters and magnetic field.

Chertok, Grechnev, and Meshalkina (2009) stated steeper slopes of the proton spectra in the 10 – 100 MeV range for non-flare-associated SEPs. This was confirmed by Gopalswamy *et al.* (2015) who estimated for four such proton events the time-of-maximum energy-spectrum index from −4.15 to −4.69 (the latter for our event). On the other hand, Mewaldt *et al.* (2012) found for the proton fluence spectra in large SEP events and GLEs a double power-law shape with a typical break energy from 10 to 100 MeV. The spectral slopes are mostly between −1 and −2 below the break energies and noticeably steeper above them. The double power-law shape is also typical of time-of-maximum spectra of many proton events (Logachev *et al.*, 2016; see also different catalogs accessible online at www.wdcb.ru/stp/solar/solar_proton_events.html). Probably, the breaks in the spectra of non-flare-associated SEPs are absent or occur at lower energies.

Light on the possible difference in the proton spectra may shed a scenario for the escape of flare-accelerated particles proposed by Masson, Antiochos, and DeVore (2013) that seems to agree with theoretical considerations, being supported in observational studies (Kocharov *et al.*, 2017; Grechnev *et al.*, 2017). In the course of reconnection that augments the poloidal flux in a flux-rope progenitor and creates the post-eruption arcade (e.g. Longcope and Beveridge, 2007; Vršnak, 2008, 2016), flare-accelerated electrons and protons are injected both down, into the flare loops, and up, into the forming flux rope. The particles confined in the flux rope are governed by the processes occurring in a magnetic trap, which rapidly expands in this situation. Coulomb collisions in a dense expanding flux rope deplete the low-energy

part of trapped particles (e.g. Metcalf and Alexander, 1999). Most electrons brake and collisionally heat the erupting prominence, i.e. CME core (Glesener *et al.*, 2013; Grechnev *et al.*, 2019); some higher-energy electrons escape collisions and remain confined, manifesting in Type IV radio emission. When the expanding flux rope encounters an open structure (streamer or coronal hole) with an antiparallel magnetic field, reconnection between them releases trapped particles into the interplanetary space.

While processes in a static or collapsing magnetic trap have been extensively addressed (e.g. Aschwanden, 2004; Bogachev and Somov, 2005, 2009), properties of electrons and protons confined in a rapidly expanding trap need a special study. The scenario outlined leads to the following qualitative expectations:

i) Near-Earth proton enhancements are not expected after confined flares.
ii) If the release of flare-accelerated protons is flux-rope-mediated, then depletion of their low-energy spectral part is expected because of Coulomb collisions in the flux rope. Most of different ideas also relate the lower-energy flattening to transport effects (Mewaldt *et al.*, 2012). The original spectral index seems to be closer to the slope above the break energy that is less influenced by transport effects and should be used to minimize their contribution (cf. Xu, Li, and Ding, 2017). Distortions caused by Coulomb collisions in dense plasma are not expected for the spectrum of shock-accelerated protons.
iii) Coulomb collisions in a dense flux rope modify the electron-to-proton ratio that Cliver (2016) and Cliver *et al.* (2019) considered. For example, the lifetime for 100 MeV protons is two orders of magnitude longer than for 0.5 MeV electrons in the same plasma. The electron-to-proton ratio escaping from a flux rope where the initial density is $> 10^{10}$ cm^{-3} may be much less than when they escape from the flare site directly (Grechnev *et al.*, 2017).
iv) A bunched release of protons accumulated in a flux rope accounts for a higher correlation between the fluences of protons and flare emissions than between their peak fluxes, as Grechnev *et al.* (2015a, 2017) found. A prompt onset of the proton flux at high energies is expected here and a shorter rise time, both of which are entirely determined by the propagation in the interplanetary space and can be quite short in a well-connected event.
v) The release of flare-accelerated protons is expected to be delayed because of the flux-rope expansion until reconnection, unlike protons that can be accelerated earlier by a shock wave in the low corona. This expectation is possibly supported by a conclusion of Ding, Jiang, and Li (2016) about two SEP releases in a GLE event, where the second release produced a double power-law spectrum (the authors' interpretation was different). This circumstance may revert the meaning of the results obtained by Reames (2009) that were interpreted in favor of the shock-accelerated origin of GLEs. The Sep29 event is present in the SEP catalogs by Paassilta *et al.* (2017, 2018); however, the onset of the SEP event was missed on SOHO, protons were not detected on STEREO-A, while the proton release time estimated from STEREO-B data is several hours later than protons were detected near Earth. Besides, the velocity dispersion analysis that is widely used in such estimations may not help in a situation, when higher-energy protons arrive later than lower-energy protons, that was the case in this event.

Section 6 has confirmed that the reconnection flux in the Sep29 event was considerable and determined the high CME speed, being comparable with a typical value in geoeffective flare-associated eruptions and even in a GLE event. This result disfavors the idea of Kahler *et al.* (2017) and Cliver *et al.* (2019) to recognize the roles of shock waves and flares in SEP

events from the reconnection flux. Moreover, such properties of SEPs as a delayed particle release time and reduced electron-to-proton ratio do not seem to be reliable indications of the shock-acceleration and need rethinking in view of recent studies.

7. Summary

Our analysis complements the picture of a geoeffective eruption of a huge quiescent prominence on 29 September 2013 that several preceding studies addressed. SDO, SOHO, and STEREO observations presented a view from different vantage points on the prominence eruption and expansion of structural components of the CME. These observations allowed us to follow the CME development, to measure the kinematics of its components, and to outline without 3D reconstructions some expectations for a possible arrival of the corresponding ICME at the Earth orbit. Next, combining the radio data from ground-based and space-borne spectrographs with solar observations, we followed the history of a shock wave excited by this eruption up to the kilometric range. ACE presented in situ measurements of the ICME in the near-Earth interplanetary space. Analysis of the whole observational data set led to the following results:

i) The CME-core progenitor was the eruptive prominence that comprised three segments. Reconnection probably combined them that drove the eruption (the dual-filament model). Some connections of the segments' ends to the solar surface survived. The segmented structure determined the behavior of the core that pressed the frontal structure from inside.
ii) The main acceleration of the prominence and CME components occurred during the eruption nearly simultaneously with a maximum of the reconnection rate measured by Cliver *et al.* (2019) that confirms the responsibility of reconnection for the eruption. The northern CME-core segment additionally accelerated two hours later at a distance of about 8 $R_\odot$ that indicates an ongoing CME formation during expansion. Similar observation was reported by Kuzmenko and Grechnev (2017).
iii) Comparing plane-of-the-sky images of the erupting prominence with the radial component of the extrapolated magnetic field, we estimated its kinematics in the radial direction. The final deprojected speeds were 930 $\mathrm{km\,s^{-1}}$ for the prominence top and 1305 $\mathrm{km\,s^{-1}}$ for the frontal structure, and the tilt of their axis to the Sun–Earth line was 39°. The results provided by this technique agree with 3D model reconstructions.
iv) The shock wave was most likely impulsively excited as a piston-shock by the erupting prominence in the same scenario as in flare-associated events and changed to the bow-shock regime later. The trajectory of Type II signatures was reproduced from 30 MHz to 70 kHz. Interruptions in the Type II emission were probably caused by propagation effects.
v) The analysis of the in situ measurements on ACE confirms the expectations for the magnetic-field variations in the ICME inferred from solar observations. The fast ICME produced by the 29 September 2013 event probably reconnected with a preceding slow ICME, whose solar source is not known. The expected outcome of reconnection is a decrease in the magnetic flux.
vi) Traditional hypotheses invoked in studies of SEP events need rethinking in view of recent studies. Such properties of SEPs as a delayed release time and reduced electron-to-proton ratio do not seem to be reliable indications of the shock-acceleration. Also, the reconnection flux unlikely can help in distinguishing between the shock-accelerated and flare-accelerated SEPs.

vii) The high speed of this non-flare-associated CME was due to a considerable reconnected flux. Estimations based on different approaches showed it to be comparable with a typical reconnection flux in flare-associated eruptions.
viii) The reconnection magnetic flux in non-flare-associated events can be considerably underestimated. It seems more promising to evaluate it from observations of coronal arcades at different stages of their development than from flare ribbons visible in 1600 Å. The 304 Å images are also helpful.

In accordance with a number of studies, the reconnection flux appears to determine the CME speed and geospace disturbances that it can cause. This is also related to the proton outcome of an eruptive event, as Kahler *et al.* (2017) proposed. This approach with refined reconnection-flux measurements is certainly promising in studies of solar eruptive events and their proton production. However, it does not seem possible to distinguish the contributions to SEPs from flare processes and shock waves based on the reconnection flux, because reconnection processes govern both the flare development and CME kinematics. For this reason, the untangling of the two contributions turns out to be a more complex problem than it seemed previously. Nevertheless, some indications of the SEP sources may exist. Results of recent studies considered critically may help to approach the solution to this complex problem.

Acknowledgements We thank A.K. Kochanov, A.M. Uralov, A.V. Belov, and I.M. Chertok for their assistance and fruitful discussions. We thank the anonymous reviewer for valuable remarks.

V. Grechnev (Sections 3.3, 4.3, 5, and 6) was funded by the Russian Science Foundation under grant 18-12-00172; the development of the methods used in Sections 3.3 and 6.2 was supported by the Program of Basic Research of the RAS Presidium No. 28. I. Kuzmenko (Sections 2, 3.1, 3.2, 4.1, and 4.2) was supported by the Russian State Contract No. 075-00389-19-00.

We appreciate the NASA/SDO and the AIA and HMI science teams; the NASA's STEREO/SECCHI science and instrument teams; the teams operating LASCO on SOHO, STEREO/WAVES, Wind/WAVES, the GOES satellites, and the Space Weather Services Culgoora Solar Observatory for the data used here. SOHO is a project of international cooperation between ESA and NASA. We thank the ACE SWEPAM, SWICS, and MAG instrument teams and the ACE Science Center for providing the ACE data. We are grateful to the team maintaining the CME Catalogs at the CDAW Data Center by NASA and the Catholic University of America in cooperation with the Naval Research Laboratory.

Disclosure of Potential Conflicts of Interest The authors declare that they have no conflicts of interest.

References

Afanasyev, A.N., Uralov, A.M., Grechnev, V.V.: 2013, Propagation of a fast magnetoacoustic shock wave in the magnetosphere of an active region. *Astron. Rep.* **57**, 594. DOI. ADS.

Al-Hamadani, F., Pohjolainen, S., Valtonen, E.: 2017, Origin of radio enhancements in Type II bursts in the outer corona. *Solar Phys.* **292**(9), 127. DOI. ADS.

Aschwanden, M.J.: 2004, *Physics of the Solar Corona. An Introduction*, Praxis Publishing Ltd., Chichester. Chapter 12. ADS.

Bogachev, S.A., Somov, B.V.: 2005, Comparison of the Fermi and betatron acceleration efficiencies in collapsing magnetic traps. *Astron. Lett.* **31**(8), 537. DOI. ADS.

Bogachev, S.A., Somov, B.V.: 2009, Effect of Coulomb collisions on the particle acceleration in collapsing magnetic traps. *Astron. Lett.* **35**(1), 57. DOI. ADS.

Bothmer, V., Mrotzek, N.: 2017, Comparison of CME and ICME structures derived from remote-sensing and in situ observations. *Solar Phys.* **292**(11), 157. DOI. ADS.

Bougeret, J.-L., Kaiser, M.L., Kellogg, P.J., Manning, R., Goetz, K., Monson, S.J., Monge, N., Friel, L., Meetre, C.A., Perche, C., Sitruk, L., Hoang, S.: 1995, Waves: The radio and plasma wave investigation on the Wind spacecraft. *Space Sci. Rev.* **71**(1-4), 231. DOI. ADS.

Bougeret, J.L., Goetz, K., Kaiser, M.L., Bale, S.D., Kellogg, P.J., Maksimovic, M., Monge, N., Monson, S.J., Astier, P.L., Davy, S., *et al.*: 2008, S/WAVES: The radio and plasma wave investigation on the STEREO mission. *Space Sci. Rev.* **136**, 487. DOI. ADS.

Cane, H.V., Erickson, W.C.: 2005, Solar Type II radio bursts and IP Type II events. *Astrophys. J.* **623**(2), 1180. DOI. ADS.

Chen, J., Krall, J.: 2003, Acceleration of coronal mass ejections. *J. Geophys. Res. Space Phys.* **108**, 1410. DOI. ADS.

Chertok, I.M., Grechnev, V.V., Abunin, A.A.: 2017, An early diagnostics of the geoeffectiveness of solar eruptions from photospheric magnetic flux observations: The transition from SOHO to SDO. *Solar Phys.* **292**, 62. DOI. ADS.

Chertok, I.M., Grechnev, V.V., Meshalkina, N.S.: 2009, On the correlation between spectra of solar microwave bursts and proton fluxes near the Earth. *Astron. Rep.* **53**(11), 1059. DOI. ADS.

Chertok, I.M., Grechnev, V.V., Uralov, A.M.: 2009, Large-scale phenomena on the Sun associated with the eruption of filaments outside active regions: The event of September 12, 1999. *Astron. Rep.* **53**(4), 355. DOI. ADS.

Chertok, I.M., Grechnev, V.V., Belov, A.V., Abunin, A.A.: 2013, Magnetic flux of EUV arcade and dimming regions as a relevant parameter for early diagnostics of solar eruptions – Sources of non-recurrent geomagnetic storms and Forbush decreases. *Solar Phys.* **282**(1), 175. DOI. ADS.

Chertok, I.M., Abunina, M.A., Abunin, A.A., Belov, A.V., Grechnev, V.V.: 2015, Relationship between the magnetic flux of solar eruptions and the Ap index of geomagnetic storms. *Solar Phys.* **290**(2), 627. DOI. ADS.

Cliver, E.W.: 2016, Flare vs. shock acceleration of high-energy protons in solar energetic particle events. *Astrophys. J.* **832**(2), 128. DOI. ADS.

Cliver, E.W., Kahler, S.W., Kazachenko, M., Shimojo, M.: 2019, The disappearing solar filament of 2013 September 29 and its large associated proton event: Implications for particle acceleration at the Sun. *Astrophys. J.* **877**(1), 11. DOI. ADS.

Démoulin, P.: 2010, Interaction of ICMEs with the solar wind. In: Maksimovic, M., Issautier, K., Meyer-Vernet, N., Moncuquet, M., Pantellini, F. (eds.) *Twelfth International Solar Wind Conference*, *Am. Inst. Phys. Conf. Ser.* **1216**, 329. DOI. ADS.

Ding, L.-G., Jiang, Y., Li, G.: 2016, Are there two distinct solar energetic particle releases in the 2012 May 17 ground level enhancement event? *Astrophys. J.* **818**(2), 169. DOI. ADS.

Domingo, V., Fleck, B., Poland, A.I.: 1995, The SOHO mission: An overview. *Solar Phys.* **162**, 1. DOI. ADS.

Fainshtein, V.G., Egorov, Y.I.: 2019, Onset of a CME-related shock within the Large-Angle Spectrometric Coronagraph (LASCO) field of view. *Solar Phys.* **294**(9), 126. DOI. ADS.

Filippov, B.P., Gopalswamy, N., Lozhechkin, A.V.: 2001, Non-radial motion of eruptive filaments. *Solar Phys.* **203**, 119. DOI. ADS.

Filippov, B.P., Gopalswamy, N., Lozhechkin, A.V.: 2002, Motion of an eruptive prominence in the solar corona. *Astron. Rep.* **46**, 417. DOI. ADS.

Filippov, B., Koutchmy, S.: 2008, Causal relationships between eruptive prominences and coronal mass ejections. *Ann. Geophys.* **26**, 3025. DOI. ADS.

Fletcher, L., Hudson, H.: 2001, The magnetic structure and generation of EUV flare ribbons. *Solar Phys.* **204**, 69. DOI. ADS.

Glesener, L., Krucker, S., Bain, H.M., Lin, R.P.: 2013, Observation of heating by flare-accelerated electrons in a solar coronal mass ejection. *Astrophys. J. Lett.* **779**, L29. DOI. ADS.

Gloeckler, G., Geiss, J., Balsiger, H., Bedini, P., Cain, J.C., Fischer, J., Fisk, L.A., Galvin, A.B., Gliem, F., Hamilton, D.C., *et al.*: 1992, The Solar Wind Ion Composition Spectrometer. *Astron. Astrophys. Suppl. Ser.* **92**(2), 267. ADS.

Gopalswamy, N., Mäkelä, P., Akiyama, S., Yashiro, S., Xie, H., Thakur, N., Kahler, S.W.: 2015, Large solar energetic particle events associated with filament eruptions outside of active regions. *Astrophys. J.* **806**(1), 8. DOI. ADS.

Gopalswamy, N., Yashiro, S., Akiyama, S., Xie, H.: 2017, Estimation of reconnection flux using post-eruption arcades and its relevance to magnetic clouds at 1 AU. *Solar Phys.* **292**(4), 65. DOI. ADS.

Grechnev, V.V., Uralov, A.M., Zandanov, V.G., Baranov, N.Y., Shibasaki, K.: 2006, Observations of prominence eruptions with two radioheliographs, SSRT, and NoRH. *Publ. Astron. Soc. Japan* **58**, 69. DOI. ADS.

Grechnev, V.V., Uralov, A.M., Slemzin, V.A., Chertok, I.M., Kuzmenko, I.V., Shibasaki, K.: 2008, Absorption phenomena and a probable blast wave in the 13 July 2004 eruptive event. *Solar Phys.* **253**(1-2), 263. DOI. ADS.

Grechnev, V.V., Uralov, A.M., Chertok, I.M., Kuzmenko, I.V., Afanasyev, A.N., Meshalkina, N.S., Kalashnikov, S.S., Kubo, Y.: 2011, Coronal shock waves, EUV waves, and their relation to CMEs. I. Reconciliation of "EIT waves", Type II radio bursts, and leading edges of CMEs. *Solar Phys.* **273**, 433. DOI. ADS.

Grechnev, V.V., Meshalkina, N.S., Chertok, I.M., Kiselev, V.I.: 2013, Relations between strong high-frequency microwave bursts and proton events. *Publ. Astron. Soc. Japan* **65**, S4. DOI. ADS.

Grechnev, V.V., Uralov, A.M., Chertok, I.M., Slemzin, V.A., Filippov, B.P., Egorov, Y.I., Fainshtein, V.G., Afanasyev, A.N., Prestage, N.P., Temmer, M.: 2014, A challenging solar eruptive event of 18 November 2003 and the causes of the 20 November geomagnetic superstorm. II. CMEs, shock waves, and drifting radio bursts. *Solar Phys.* **289**, 1279. DOI. ADS.

Grechnev, V.V., Kiselev, V.I., Meshalkina, N.S., Chertok, I.M.: 2015a, Relations between microwave bursts and near-Earth high-energy proton enhancements and their origin. *Solar Phys.* **290**(10), 2827. DOI. ADS.

Grechnev, V.V., Uralov, A.M., Kuzmenko, I.V., Kochanov, A.A., Chertok, I.M., Kalashnikov, S.S.: 2015b, Responsibility of a filament eruption for the initiation of a flare, CME, and blast wave, and its possible transformation into a bow shock. *Solar Phys.* **290**, 129. DOI. ADS.

Grechnev, V.V., Uralov, A.M., Kochanov, A.A., Kuzmenko, I.V., Prosovetsky, D.V., Egorov, Y.I., Fainshtein, V.G., Kashapova, L.K.: 2016, A tiny eruptive filament as a flux-rope progenitor and driver of a large-scale CME and wave. *Solar Phys.* **291**, 1173. DOI. ADS.

Grechnev, V.V., Kiselev, V.I., Uralov, A.M., Klein, K.-L., Kochanov, A.A.: 2017, The 26 December 2001 solar eruptive event responsible for GLE63: III. CME, shock waves, and energetic particles. *Solar Phys.* **292**, 102. DOI. ADS.

Grechnev, V.V., Lesovoi, S.V., Kochanov, A.A., Uralov, A.M., Altyntsev, A.T., Gubin, A.V., Zhdanov, D.A., Ivanov, E.F., Smolkov, G.Y., Kashapova, L.K.: 2018, Multi-instrument view on solar eruptive events observed with the Siberian Radioheliograph: From detection of small jets up to development of a shock wave and CME. *J. Atmos. Solar-Terr. Phys.* **174**, 46. DOI. ADS.

Grechnev, V.V., Kochanov, A.A., Uralov, A.M., Slemzin, V.A., Rodkin, D.G., Goryaev, F.F., Kiselev, V.I., Myshyakov, I.I.: 2019, Development of a fast CME and properties of a related interplanetary transient. *Solar Phys.* **294**(10), 139. DOI. ADS.

Guidice, D.A.: 1979, Sagamore Hill Radio Observatory, Air Force Geophysics Laboratory, Hanscom Air Force Base, Massachusetts 01731. Report. *Bull. Am. Astron. Soc.* **11**, 311. ADS.

Guidice, D.A., Cliver, E.W., Barron, W.R., Kahler, S.: 1981, The air force RSTN system. *Bull. Am. Astron. Soc.* **13**, 553. ADS.

Holman, G.D., Foord, A.: 2015, Direct spatial association of an X-ray flare with the eruption of a solar quiescent filament. *Astrophys. J.* **804**(2), 108. DOI. ADS.

Inhester, B., Birn, J., Hesse, M.: 1992, The evolution of line tied coronal arcades including a converging footpoint motion. *Solar Phys.* **138**(2), 257. DOI. ADS.

Kahler, S.W., Kazachenko, M., Lynch, B.J., Welsch, B.T.: 2017, Flare magnetic reconnection fluxes as possible signatures of flare contributions to gradual SEP events. In: *J. Phys. Conf. Ser.* **900**, 012011. DOI. ADS.

Kaiser, M.L., Kucera, T.A., Davila, J.M., St. Cyr, O.C., Guhathakurta, M., Christian, E.: 2008, The STEREO mission: An introduction. *Space Sci. Rev.* **136**, 5. DOI. ADS.

Kallenrode, M.-B.: 2003, Current views on impulsive and gradual solar energetic particle events. *J. Phys. G, Nucl. Phys.* **29**, 965. ADS.

Klein, K.-L., Trottet, G.: 2001, The origin of solar energetic particle events: Coronal acceleration versus shock wave acceleration. *Space Sci. Rev.* **95**, 215. ADS.

Knock, S.A., Cairns, I.H.: 2005, Type II radio emission predictions: Sources of coronal and interplanetary spectral structure. *J. Geophys. Res. Space Phys.* **110**(A1), A01101. DOI. ADS.

Kocharov, L., Pohjolainen, S., Mishev, A., Reiner, M.J., Lee, J., Laitinen, T., Didkovsky, L.V., Pizzo, V.J., Kim, R., Klassen, A., Karlicky, M., Cho, K.-S., Gary, D.E., Usoskin, I., Valtonen, E., Vainio, R.: 2017, Investigating the origins of two extreme solar particle events: Proton source profile and associated electromagnetic emissions. *Astrophys. J.* **839**(2), 79. DOI. ADS.

Kuzmenko, I.V., Grechnev, V.V.: 2017, Development and parameters of a non-self-similar CME caused by the eruption of a quiescent prominence. *Solar Phys.* **292**, 143. DOI.

Kwon, R.-Y., Zhang, J., Olmedo, O.: 2014, New insights into the physical nature of coronal mass ejections and associated shock waves within the framework of the three-dimensional structure. *Astrophys. J.* **794**, 148. DOI. ADS.

Kwon, R.-Y., Zhang, J., Vourlidas, A.: 2015, Are halo-like solar coronal mass ejections merely a matter of geometric projection effects? *Astrophys. J. Lett.* **799**, L29. DOI. ADS.

Lemen, J.R., Title, A.M., Akin, D.J., Boerner, P.F., Chou, C., Drake, J.F., Duncan, D.W., Edwards, C.G., Friedlaender, F.M., Heyman, G.F., *et al.*: 2012, The Atmospheric Imaging Assembly (AIA) on the Solar Dynamics Observatory (SDO). *Solar Phys.* **275**, 17. DOI. ADS.

Li, T., Zhang, J., Ji, H.: 2015, Filament activation in response to magnetic flux emergence and cancellation in filament channels. *Solar Phys.* **290**(6), 1687. DOI. ADS.

Liu, Y., Hoeksema, J.T., Scherrer, P.H., Schou, J., Couvidat, S., Bush, R.I., Duvall, T.L., Hayashi, K., Sun, X., Zhao, X.: 2012, Comparison of line-of-sight magnetograms taken by the Solar Dynamics Observatory/Helioseismic and Magnetic Imager and Solar and Heliospheric Observatory/Michelson Doppler Imager. *Solar Phys.* **279**(1), 295. DOI. ADS.

Logachev, Y.I., Bazilevskaya, G.A., Vashenyuk, E.V., Daibog, E.I., Ishkov, V.N., Lazutin, L.L., Miroshnichenko, L.I., Nazarova, M.N., Petrenko, I.E., Stupishin, A.G., Surova, G.M., Yakovchuk, O.S.: 2016, *Catalogue of Solar Proton Events in the 23rd Cycle of Solar Activity*, Geophysical Center RAS, Moscow. DOI. www.gcras.ru/eng/.

Longcope, D.W., Beveridge, C.: 2007, A quantitative, topological model of reconnection and flux rope formation in a two-ribbon flare. *Astrophys. J.* **669**(1), 621. DOI. ADS.

MacQueen, R.M., Fisher, R.R.: 1983, The kinematics of solar inner coronal transients. *Solar Phys.* **89**(1), 89. DOI. ADS.

Manchester, W., Kilpua, E.K.J., Liu, Y.D., Lugaz, N., Riley, P., Török, T., Vršnak, B.: 2017, The physical processes of CME/ICME evolution. *Space Sci. Rev.* **212**, 1159. DOI. ADS.

Masson, S., Antiochos, S.K., DeVore, C.R.: 2013, A model for the escape of solar-flare-accelerated particles. *Astrophys. J.* **771**, 82. DOI. ADS.

McComas, D.J., Bame, S.J., Barker, P., Feldman, W.C., Phillips, J.L., Riley, P., Griffee, J.W.: 1998, Solar Wind Electron Proton Alpha Monitor (SWEPAM) for the Advanced Composition Explorer. *Space Sci. Rev.* **86**, 563. DOI. ADS.

Metcalf, T.R., Alexander, D.: 1999, Coronal trapping of energetic flare particles: Yohkoh/HXT observations. *Astrophys. J.* **522**, 1108. DOI. ADS.

Mewaldt, R.A., Looper, M.D., Cohen, C.M.S., Haggerty, D.K., Labrador, A.W., Leske, R.A., Mason, G.M., Mazur, J.E., von Rosenvinge, T.T.: 2012, Energy spectra, composition, and other properties of ground-level events during Solar Cycle 23. *Space Sci. Rev.* **171**(1 – 4), 97. DOI. ADS.

Miklenic, C.H., Veronig, A.M., Vršnak, B.: 2009, Temporal comparison of nonthermal flare emission and magnetic-flux change rates. *Astron. Astrophys.* **499**(3), 893. DOI. ADS.

Paassilta, M., Raukunen, O., Vainio, R., Valtonen, E., Papaioannou, A., Siipola, R., Riihonen, E., Dierckxsens, M., Crosby, N., Malandraki, O., Heber, B., Klein, K.-L.: 2017, Catalogue of 55 – 80 MeV solar proton events extending through Solar Cycles 23 and 24. *J. Space Weather Space Clim.* **7**, A14. DOI. ADS.

Paassilta, M., Papaioannou, A., Dresing, N., Vainio, R., Valtonen, E., Heber, B.: 2018, Catalogue of $>$ 55 MeV wide-longitude solar proton events observed by SOHO, ACE, and the STEREOs at $\approx$ 1 AU during 2009 – 2016. *Solar Phys.* **293**(4), 70. DOI. ADS.

Pal, S., Nandy, D., Srivastava, N., Gopalswamy, N., Panda, S.: 2018, Dependence of coronal mass ejection properties on their solar source active region characteristics and associated flare reconnection flux. *Astrophys. J.* **865**(1), 4. DOI. ADS.

Palacios, J., Cid, C., Guerrero, A., Saiz, E., Cerrato, Y.: 2015, Supergranular-scale magnetic flux emergence beneath an unstable filament. *Astron. Astrophys.* **583**, A47. DOI. ADS.

Pohjolainen, S., Hori, K., Sakurai, T.: 2008, Radio bursts associated with flare and ejecta in the 13 July 2004 event. *Solar Phys.* **253**(1-2), 291. DOI. ADS.

Prestage, N.P., Luckhurst, R.G., Paterson, B.R., Bevins, C.S., Yuile, C.G.: 1994, A new radio spectrograph at Culgoora. *Solar Phys.* **150**(1 – 2), 393. DOI. ADS.

Qiu, J., Yurchyshyn, V.B.: 2005, Magnetic reconnection flux and coronal mass ejection velocity. *Astrophys. J. Lett.* **634**(1), L121. DOI. ADS.

Qiu, J., Hu, Q., Howard, T.A., Yurchyshyn, V.B.: 2007, On the magnetic flux budget in low-corona magnetic reconnection and interplanetary coronal mass ejections. *Astrophys. J.* **659**, 758. DOI. ADS.

Reames, D.V.: 2009, Solar release times of energetic particles in ground-level events. *Astrophys. J.* **693**(1), 812. DOI. ADS.

Reames, D.V.: 2013, The two sources of solar energetic particles. *Space Sci. Rev.* **175**, 53. DOI. ADS.

Reiner, M.J., Vourlidas, A., Cyr, O.C.S., Burkepile, J.T., Howard, R.A., Kaiser, M.L., Prestage, N.P., Bougeret, J.-L.: 2003, Constraints on coronal mass ejection dynamics from simultaneous radio and white-light observations. *Astrophys. J.* **590**(1), 533. DOI. ADS.

Richardson, I.G., Cane, H.V.: 2010, Near-Earth interplanetary coronal mass ejections during Solar Cycle 23 (1996 – 2009): Catalog and summary of properties. *Solar Phys.* **264**, 189. DOI. ADS.

Rouillard, A.P., Plotnikov, I., Pinto, R.F., Tirole, M., Lavarra, M., Zucca, P., Vainio, R., Tylka, A.J., Vourlidas, A., De Rosa, M.L., *et al.*: 2016, Deriving the properties of coronal pressure fronts in 3D: Application to the 2012 May 17 ground level enhancement. *Astrophys. J.* **833**, 45. DOI. ADS.

Saito, K., Makita, M., Nishi, K., Hata, S.: 1970, A non-spherical axisymmetric model of the solar K corona of the minimum type. *Ann. Tokyo Astron. Obs.* **12**, 53. ADS.

Scherrer, P.H., Bogart, R.S., Bush, R.I., Hoeksema, J.T., Kosovichev, A.G., Schou, J., Rosenberg, W., Springer, L., Tarbell, T.D., Title, A., *et al.*: 1995, The Solar Oscillations Investigation – Michelson Doppler Imager. *Solar Phys.* **162**(1 – 2), 129. DOI. ADS.

Scherrer, P.H., Schou, J., Bush, R.I., Kosovichev, A.G., Bogart, R.S., Hoeksema, J.T., Liu, Y., Duvall, T.L., Zhao, J., Title, A.M., *et al.*: 2012, The Helioseismic and Magnetic Imager (HMI) investigation for the Solar Dynamics Observatory (SDO). *Solar Phys.* **275**, 207. DOI. ADS.

Smith, C.W., L'Heureux, J., Ness, N.F., Acuña, M.H., Burlaga, L.F., Scheifele, J.: 1998, The ACE magnetic fields experiment. *Space Sci. Rev.* **86**, 613. DOI. ADS.

Stone, E.C., Frandsen, A.M., Mewaldt, R.A., Christian, E.R., Margolies, D., Ormes, J.F., Snow, F.: 1998, The Advanced Composition Explorer. *Space Sci. Rev.* **86**, 1. DOI. ADS.

Švestka, Z.: 2001, Varieties of coronal mass ejections and their relation to flares. *Space Sci. Rev.* **95**, 135. ADS.

Temmer, M., Veronig, A.M., Vršnak, B., Rybák, J., Gömöry, P., Stoiser, S., Maričić, D.: 2008, Acceleration in fast halo CMEs and synchronized flare HXR bursts. *Astrophys. J. Lett.* **673**(1), L95. DOI. ADS.

Temmer, M., Veronig, A.M., Kontar, E.P., Krucker, S., Vršnak, B.: 2010, Combined STEREO/RHESSI study of coronal mass ejection acceleration and particle acceleration in solar flares. *Astrophys. J.* **712**(2), 1410. DOI. ADS.

Uralov, A.M., Lesovoi, S.V., Zandanov, V.G., Grechnev, V.V.: 2002, Dual-filament initiation of a coronal mass ejection: Observations and model. *Solar Phys.* **208**(1), 69. DOI. ADS.

Uralova, S.V., Uralov, A.M.: 1994, WKB approach to the problem of magnetohydrodynamic shock propagation through the heliospheric current sheet. *Solar Phys.* **152**(2), 457. DOI. ADS.

Vršnak, B.: 2008, Processes and mechanisms governing the initiation and propagation of CMEs. *Ann. Geophys.* **26**(10), 3089. DOI. ADS.

Vršnak, B.: 2016, Solar eruptions: The CME-flare relationship. *Astron. Nachr.* **337**(10), 1002. DOI. ADS.

Vršnak, B., Cliver, E.W.: 2008, Origin of coronal shock waves. Invited review. *Solar Phys.* **253**, 215. DOI. ADS.

Wood, B.E., Lean, J.L., McDonald, S.E., Wang, Y.-M.: 2016, Comparative ionospheric impacts and solar origins of nine strong geomagnetic storms in 2010 – 2015. *J. Geophys. Res.* **121**(6), 4938. DOI. ADS.

Xu, Z.G., Li, C., Ding, M.D.: 2017, Observations of a coronal shock wave and the production of solar energetic particles. *Astrophys. J.* **840**(1), 38. DOI. ADS.

Yashiro, S., Gopalswamy, N., Michalek, G., St. Cyr, O.C., Plunkett, S.P., Rich, N.B., Howard, R.A.: 2004, A catalog of white light coronal mass ejections observed by the SOHO spacecraft. *J. Geophys. Res. Space Phys.* **109**, A07105. DOI. ADS.

Yermolaev, Y.I., Nikolaeva, N.S., Lodkina, I.G., Yermolaev, M.Y.: 2012, Geoeffectiveness and efficiency of CIR, sheath, and ICME in generation of magnetic storms. *J. Geophys. Res. Space Phys.* **117**, A00L07. DOI. ADS.

Zhang, J., Dere, K.P., Howard, R.A., Kundu, M.R., White, S.M.: 2001, On the temporal relationship between coronal mass ejections and flares. *Astrophys. J.* **559**, 452. DOI. ADS.